Accepted Manuscript

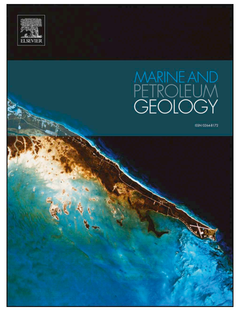

Examining fault architecture and strain distribution using geospatial and geomechanical modelling: An example from the Qaidam basin, NE Tibet

Yangwen Pei, Douglas A. Paton, Rob J. Knipe, Kongyou Wu

PII: S0264-8172(17)30109-5

DOI: 10.1016/j.marpetgeo.2017.03.023

Reference: JMPG 2861

To appear in: *Marine and Petroleum Geology*

Received Date: 7 November 2016

Revised Date: 23 February 2017

Accepted Date: 22 March 2017

Please cite this article as: Pei, Y., Paton, D.A., Knipe, R.J., Wu, K., Examining fault architecture and strain distribution using geospatial and geomechanical modelling: An example from the Qaidam basin, NE Tibet, *Marine and Petroleum Geology* (2017), doi: 10.1016/j.marpetgeo.2017.03.023.

Examining Fault Architecture and Strain Distribution using Geospatial and Geomechanical Modelling: an example from the Qaidam Basin, NE Tibet

Yangwen Pei[a, b, *], Douglas A. Paton[b], Rob J. Knipe[b], Kongyou Wu[a]

[a] School of Geosciences, China University of Petroleum, Qingdao, Shandong Province, 266580, China

[b] School of Earth & Environment, University of Leeds, Leeds, West Yorkshire, LS2 9JT, England

* Corresponding author. Email: peiyangwen@upc.edu.cn. Tel: +8618266225617.

Abstract

The investigation of complex geological setting is still dominated by traditional geo-data collection and analytical techniques, e.g., stratigraphic logging, dip data measurements, structural ground mapping, seismic interpretation, balance section restoration, forward modelling, etc. Despite the advantages of improving our understanding in structural geometry and fault architecture, the geospatial modelling, applying computer-aided three-dimensional geometric design, visualization and interpretation, has rarely been applied to such complex geological setting. This study used the Lenghu fold-and-thrust belt (in Qaidam basin, NE Tibetan Plateau) to demonstrate that the application of geospatial and geomechanical modelling could improve our understanding and provide an effective technique for investigating the fault architecture and strain distribution. The three-dimensional configuration of the Lenghu fold-and-thrust belt was initially derived from traditional analysis techniques, such as regional stratigraphic logging, cross section construction, meso-scale ground mapping and landsat image interpretation. The high-resolution field data and landsat image were integrated to construct the geospatial model, which was subsequently used to quantitatively investigate the fault throw changes along the Lenghu thrust fault zone and to understand its control on the lateral structural variation. The geospatial model was then restored in three dimensions to reveal the kinematic evolution of the Lenghu fold-and-thrust belt. Geomechanical modelling, using a

Mass-Spring algorithm, provided an effective three-dimensional tool for structural strain analysis, which was used to predict the strain distribution throughout the overall structure, e.g., normal faults with throws ranging from meters to tens of meters in the hanging-wall. The strain distribution predicted by geomechanical modelling was then validated by the natural normal faults in the hanging-wall. The high accordance between the strain prediction and statistics of natural normal faults demonstrates good applicability of geospatial and geomechanical modelling in the complex geological setting of the Lenghu fold-and-thrust belt. The geospatial models and geomechanical models, therefore, can provide a robust technique for analyzing and interpreting multi-source data within a three-dimensional environment. We anticipate that the application of three-dimensional geospatial modelling and geomechanical modelling, integrating both multi-source geologic data and three-dimensional analytical techniques, can provide an effective workflow for investigating the fault architecture and strain distribution at different scales (e.g., ranging from regional- to meso-scale).

Keywords

geospatial modelling, geomechanical modelling, fault architecture, strain distribution prediction

1. Introduction

Seismic reflection surveying has been an effective technique for revealing subsurface structural geometry for decades. However, the limited resolution (e.g., 15-50 m) of seismic reflection apparently inhibits its effectiveness of interpreting structural features that are under seismic resolution. Given the important control of these structural features on hydrocarbon exploration, geologists realized the importance of investigating detailed stratigraphy, fold geometry, and fault architecture at meso- or even smaller scales. However, the investigation of geologically complex setting is still dominated by traditional data collection and analytical techniques, e.g., stratigraphic logging, dip data measurements, stratigraphic correlation, seismic interpretation, balance section restoration, and forward modelling. Because of the uncertainty in projection and positioning of multi-scale geo-data within a three-dimensional environment, these traditional techniques can only be used in an illustrative way. Geospatial modelling, employing computer-aided three-dimensional model construction, visualization and quantitative analysis, is rarely applied to these complex geologic settings, despite its significant advantages in improving our understanding in structural geometry and fault architecture. The application of geospatial models can provide both new insights into our understanding of such a geological setting and a robust technique for analyzing and interpreting geo-data within a three-dimensional environment. This contribution uses the Lenghu fold-and-thrust belt, an example from the Qaidam basin, NE Tibetan Plateau (Fig.1) (e.g., Mao et al., 2016; Métivier et al., 1998; Wei et al., 2016; Wu et al., 2011; Yin et al., 2008b; Yin and Harrison, 2000), to demonstrate the benefits of three-dimensional geospatial models in providing new insights into our understanding, including fold geometry, fault zone architecture, and fault throw distribution. Geomechanical modelling upon the three-dimensional geospatial models, using a Mass-Spring algorithm (e.g., Baraff and Witkin, 1998; Bourguignon and Cani, 2000; Provot, 1995; Terzopoulos et al., 1987), can also provide an effective three-dimensional tool for advanced structural strain analysis.

As an important oil-bearing fold-and-thrust belt, many previous studies have investigated the structural geometry of the Lenghu fold-and-thrust belt (e.g., Mao et al., 2016; Pei et al., 2014; Yin et al., 2008a). Using traditional data collection and analytical techniques (e.g., dip measurements, section construction, and section restoration), these studies revealed the first-order geometry of the Lenghu fold-and-thrust belt and fit this regional structure into the basin-scale geological setting. However, constrained by the limitations of these traditional data collection and analytical methods, it is difficult to evaluate the structural deformation at meso-scale. In this paper, we present a case study of applying three-dimensional geospatial modelling and geomechanical modelling to the Lenghu fold-and-thrust belt, to reveal its detailed fault architecture and strain distribution. High-resolution field data and landsat images were integrated to construct the geospatial model, which was subsequently used to quantitatively investigate the fault throw changes along the fault zone and understand its control on the lateral variation of the Lenghu fold-and-thrust belt. The geospatial model was then restored in three dimensions to reveal the structural evolution. Geomechanical modelling upon three-dimensional geospatial models allows for advanced structural strain analysis, which can be used to predict the strain distribution throughout the overall structure (e.g., normal faults with throws ranging from meters to tens of meters). The strain distribution predicted by geomechanical modelling was then validated by the natural normal faults in the hanging-wall of the Lenghu fold-and-thrust belt. High accordance between the strain prediction and statistics of natural normal faults indicates good applicability of geomechanical modelling in this complex geologic setting. With appropriate validation of field data, the reliability of the geomechanical models can be effectively tested. We anticipate that the application of three-dimensional geospatial modelling and geomechanical modelling in the Lenghu fold-and-thrust belt can provide an effective workflow for investigating both the fault architecture and strain distribution at different scales (e.g., ranging from regional- to meso-scale). This approach is particularly useful in geological setting where the traditional geo-data collection and analytical techniques are insufficient to understand the structural complexity and its geological history. The application of geospatial and geomechanical modelling can significantly improve our understanding in the complexity of structural lateral variation as well as its control on the strain distribution within a three-dimensional environment.

2. Geological Setting

The Qaidam basin, an oil/gas-bearing Mesozoic-Cenozoic sedimentary basin, is located in the northern edge of the Tibetan Plateau (Fig.1, modified after Yin et al., 2008a)(Fig.1).The Qaidam basin covers an area of ~120,000 km^2 and has an average elevation of ~3 km (Fielding, 1996). In map view, the Qaidam basin is a rhombic shaped basin, and its N-S width changes from ~150 km in the east to ~300 km in the west (e.g., Cheng et al., 2015; Cheng et al., 2014; Mao et al., 2016; Métivier et al., 1998; Wu et al., 2011; Yin et al., 2007; Yin et al., 2008a; Yin et al., 2008b). Tectonically, the Qaidam basin is bounded by the Qilian Shan-Nan Shan thrust belt to the northeast (e.g. Burchfiel et al., 1989; Gaudemer et al., 1995; Meng et al., 2001; Meyer et al., 2010; Tapponnier et al., 1990; Yin et al., 2008a; Zuza et al., 2016), the left-lateral strike-slip Altyn Tagh Fault to the northwest (e.g. Bendick et al., 2000; Cowgill, 2007; Cowgill et al., 2004a; Cowgill et al., 2004b; Meyer et al., 1998; Wittlinger et al., 1998; Yin et al., 2007; Yue et al., 2001; Yue et al., 2004), and the Qimen Tagh-Eastern Kunlun thrust belt to the southwest (e.g. Chen et al., 1999; Cheng et al., 2015; Cheng et al., 2014; Craddock et al., 2012; Jolivet et al., 2003; Meng et al., 2001; Roger et al., 2008; Yin et al., 2007). The stratigraphy of the Qaidam basin is divided into three main tectonic units, which are metamorphic basement, late Palaeozoic-Mesozoic sediments, and Cenozoic sediments (e.g., Cui et al., 1995; Deng et al., 1995; Gao et al., 1995; Xia et al., 2001). Based on outcrop observations, seismic sections, boreholes, terrestrial fossils, basin-scale stratigraphic correlation, fission-track and $^{40}Ar/^{39}Ar$ dating of detrital micas (Qiu, 2002; Rieser et al., 2006a; Rieser et al., 2006b; Song and Wang, 1993; Sun et al., 2005; Xia et al., 2001; Yang et al., 1992), the division and time assignments of Mesozoic to Cenozoic sediments were proposed, which are, in younging direction, (i). the Jurassic and locally distributed Cretaceous sediments (Jr; 206-65Ma); (ii). the Palaeocene to early Eocene Lulehe Formation (E_{1+2}; 65–49 Ma); (iii). the middle and late Eocene Lower Xiagancaigou Formation (E_{3-1}; 49–37 Ma); (iv). the early Oligocene Upper Xiagancaigou Formation (E_{3-2}; 37–28.5 Ma); (v). the late Oligocene Shanggancaigou Formation (N_1; 28.5–23.8 Ma); (vi). the early to middle Miocene Xiayoushashan Formation (N_{2-1}; 23.5–11.2 Ma); (vii). the late Miocene Shangyoushashan Formation (N_{2-2}; 11.2–5.3 Ma); (viii). the Pliocene Shizigou Formation (N_{2-3}; 5.3–1.8 Ma); (ix). the Pleistocene Qigequan Formation (Q_1; 1.8–0.01 Ma); and (x). the Holocene Dabuxun Yanqiao Formation (Q_2).

The Lenghu fold-and-thrust belt, located along the northern margin of the Qaidam basin, is an ~10 km wide asymmetric anticline controlled by the Lenghu thrust fault (Fig.1), corresponding to the regional NE-SW-trending contraction (e.g., Chen et al., 2005; Mao et al., 2016; Wang et al., 2006a). The Lenghu fold-and-thrust belt is well imaged in an ~15 km long seismic section (Fig.2) with stratigraphic constraints by the Lengke1 well. The Lengke1 well provides lithological boundaries T_6 to T_3 upward, and T_3 is duplicated by a high-angle thrust fault (~50°). The basement is a continental crust consisting of Precambrian metamorphic and granitic rocks based on the magnetotelluric sounding and deep seismic refraction data (Xia et al., 2001). Overlying the basement, six main stratigraphic units have been interpreted based on well-log data, which includes Jurassic through middle Miocene stratigraphic units. Three faults (i.e., f_1, f_2 and f_3) are interpreted based on discontinuous and truncated reflectors. The surface geology shows a broad fold (i.e., the Lenghu anticline) cut by a high-angle thrust fault through the fold axis, and the seismic reflection section suggests shallow of the Lenghu thrust fault (f_1) with increasing depth into a decollement above a sequence interpreted as the late Eocene sediments (E_3). The hanging-wall anticline extends throughout the section continuing below the Lenghu thrust fault.

In the seismic section (Fig.2), the E_{1+2} to $N_{2\text{-}1}$ units maintain constant thickness, whereas the hanging-wall Jr is approximately four times thicker compared to the footwall, suggesting growth strata relationships. Growth strata are also observed in unit $N_{2\text{-}2}$. Based on the truncational relationship between the horizons and faults, the geometry of the anticline is controlled by the lower SW-directing reverse faults (f_2 and f_3 in Fig.2) and upper younger NE-directing Lenghu thrust fault (f_1 in Fig.2). The two main faults, f_1 and f_2, account for majority of the fault throw, ~800 m in the unit Jr along f_2 and ~800 m in the unit N_1 along f_1. The fault throws of f_1 and f_2 all decrease upward along the fault planes. Previous studies proposed that the Qaidam basin experienced an earlier extension stage (i.e., Mesozoic extension) and a later contraction stage (i.e., Cenozoic contraction) (e.g., Chen et al., 2003; Pang et al., 2004; Vincent and Allen, 1999; Wang et al., 2006b; Zhu et al., 2006). The lower SW-directed reverse fault f_2 formed as a normal fault initially and then was inverted to be a reverse fault in the later contraction stage, leading to a Jr thickness difference between the hanging-wall and footwall. The constant thickness of E_{1+2}-$N_{2\text{-}1}$ in both the hanging-wall and footwall indicates the contraction started no earlier than the deposition of $N_{2\text{-}1}$. The growth strata developed in $N_{2\text{-}2}$ indicate the initiation of the anticline development. In summary, the geological history can be inferred as occurring in three main stages: (i) the initial Jurassic normal faulting related to the NE-SW oriented extension, (ii) the inverted SW-directed reverse faulting reacting to the NE-SW-trending contraction in the early Eocene (E_{1+2}), and (iii) the NE-directing reverse faulting reacting to the NE-SW-trending contraction from the late Eocene (E_3) to the Neocene (N).

3. Data and Methods

To analyze the Lenghu fold-and-thrust belt, we integrated both remote sensing data (landsat images), and field observations, which are outlined below, to derive three-dimensional geospatial models and geomechanical models using 2D/3D Move (Midland Valley, version 2013.1.1). We applied the following data collection and analysis techniques:

1) Stratigraphy logging: three well-exposed traverses (~2150 m total stratigraphic thickness) were logged to constrain the detailed stratigraphy across the Lenghu fold-and-thrust belt (Fig.3); this corresponds to ***HW1***, ***HW2*** and ***FW***, representing hanging-wall traverse 1, hanging-wall traverse 2 and footwall traverse, respectively (Fig.4).

2) Cross section construction: to investigate the spatial distribution of fault throw along the fault zone and the anticline geometry in the hanging-wall, ten parallel sections were created using 2D/3D Move (Midland Valley) based on detailed structural measurements and ground-truthed landsat image interpretation (Fig.5). The growth strata were only observed in N_{2-2} unit in the further hanging-wall and footwall in the seismic section (Fig.2). Therefore, for the cross section covering the vicinity of the Lenghu thrust fault, it was assumed that layer stratigraphy with

constant thickness was appropriate based on the continuous stratigraphic units (i.e., N_{2-1}) that were mapped out on the landsat image and the stratigraphic logs.

3) Geospatial modelling and three-dimensional restoration: The geospatial models were constructed by integrating the field-scale observation and cross sections. The stratigraphic boundaries were extrapolated above the present topography to predict the thrust fault cut-off positions, which were subsequently used to estimate the minimal throw of the fault zone (Fig.6). The spatial distribution of fault throws and lateral variation of hanging-wall anticline were then quantitatively analyzed to understand the three-dimensional fault architecture of the Lenghu fold-and-thrust belt. The geospatial model was then restored in three dimensions (using 3D Move, Midland Valley) to reveal the structural evolution of the Lenghu fold-and-thrust belt (Fig.7).

4) Geomechanical modelling and Strain analysis: Geomechanical modelling, using a Mass-Spring algorithm, provides an effective three-dimensional tool for model validation and advanced structural strain analysis (Fig.8). After Mass-Spring restoration upon the geospatial model, using 3D Move of Midland Valley, the resultant strain distribution in the Lenghu fold-and-thrust belt was investigated to predict the distribution of minor structures. Statistics of natural normal faults in the Lenghu fold-and-thrust belt were then used to validate the effectiveness of strain prediction (Fig.9 and Fig.10).

4. High-resolution Fieldwork and Geospatial Model

A seismic section, high-resolution fault system maps and detailed regional sections were integrated to study the structural geometry and fault architecture of the Lenghu fold-and-thrust belt (Fig.3, see position in Fig.1). The regional stratigraphy, fault zone geometry and minor faults distribution of the hanging-wall were all traced and logged in the high-resolution fieldwork. A NE-directing thrust fault zone was interpreted based on the truncated layers in the landsat image, which corresponds to the Lenghu thrust fault f_1 in the aforementioned seismic section (Fig.2). In the hanging-wall, a NW-SE-trending anticline forms as a result of the Lenghu thrust fault (yellow dash line in Fig.3). However, based on the landsat image interpretation and high-resolution ground mapping, the hanging-wall anticline does not present universal geometry along its trend, with two local culminations in the hanging-wall (green triangles in Fig.3). Based on field mapping, minor structures, such as normal faults with smaller throws in the hanging-wall and folds with smaller amplitudes in the footwall, were also identified and interpreted in the landsat image. To constrain the construction of the three-dimensional geospatial model, detailed stratigraphy was logged and high-resolution parallel sections were created to quantitatively delineate the fault architecture as well as the lateral structural variation of the Lenghu fold-and-thrust belt, particularly the fault throw distribution along the Lenghu thrust fault zone.

4.1. Stratigraphy

The detailed stratigraphy of the hanging-wall and footwall was logged on the ground along three traverses that were sub-perpendicular to strike of the Lenghu fold-and-thrust belt (Fig.3), two traverses in the hanging-wall (***HW1***: ~3 km long through the northern culmination and ***HW2***: ~1.5 km long through the southern culmination), and one traverse in the footwall (***FW***: ~3 km long through northern end of the footwall). The stratigraphic columns of ***HW1***, ***HW2*** and ***FW*** represent thicknesses of ~1200 m, ~350 m and ~650 m, respectively. The stratigraphy of ***HW1*** and ***HW2*** is similar to each other and the stratigraphic correlation between the hanging-wall and footwall suggests the division into the following five main packages (Fig.3), (i) S_a comprises fine sandstones and red/grey/mottled shales/mudstones, with a minimum thickness of ~170 m in ***HW1***; (ii) S_b includes fine-medium sandstones interbedded with very few thin red/grey mudstones and its thickness is ~350 m; (iii) S_c represents medium sandstones with inconstant thickness ranging from 10 m to 30 m; (iv) S_d, ~400 m thick, shows a similar lithology as S_b, but with thin medium-coarse sandstones interbedded; (v) S_e becomes coarse-very coarse sandstones with a thickness exceeding 250 m.

The stratigraphic correlation between the hanging-wall and footwall is used to estimate the fault displacement of the Lenghu anticline. According to the stratigraphic correlation, the fault throw is inferred to be ~500 m in the northern anticline. Therefore, the main reverse fault has a throw that is large enough to be imaged on seismic reflection data, which corresponds to the Lenghu thrust fault (f_1) in the seismic section (Fig.2). Given the northern culmination exposes less stratigraphy than the southern culmination and the exposure of the footwall stratigraphy decreases southward, it is assumed that the fault displacement increases from the northern culmination to the southern culmination. The lithology of the Lenghu anticline changes from coarse/very coarse sandstones in the two walls to clay-rich fine sandstones towards the central fault zone.

4.2. Regional transects

Based on the field observation, the southern anticline shows a higher elevation change from the hanging-wall to footwall than the northern anticline (Fig.3). The southern anticline exposes more stratigraphy in the core than the northern anticline. The larger displacement in the southern anticline leads to higher uplift of the hanging-wall and more exposure of older stratigraphy in the surface. To investigate the fault architecture and its lateral variation along the Lenghu fold-and-thrust belt, ten parallel sections (i.e., S1-S10), each with a length of ~6 km and depth of ~1.25 km, were constructed by integrating both the landsat image interpretation and field geological data (e.g., stratigraphic boundaries, ground mapping of fault traces, and dip measurements) (Fig.5, see section traces in Fig.3). The stratigraphic boundaries and fault traces are well constrained by the surface dip measurements in the interpretation and construction of the sub-surface sections. The landsat image interpretation also provides good constraints for the section construction. The ten parallel sections are evenly spaced, with an interval of ~600 m, to present both surface and sub-surface geology of the Lenghu5 fold-and-thrust belt. The ten parallel sections cover a total distance of ~5.4 km along the trend of the Lenghu thrust zone, which allows us to evaluate the fault throw distribution and its lateral variation.

The main thrust fault (**F1**, in translucent yellow) and two splay faults (**F2** in cyan and **F3** in red) were interpreted in the sections after necessary simplifications of minor structures that are presented in the plan view structural interpretation (Fig.3). The stratigraphic columns were aligned to the section surface to assist the construction of the stratigraphic boundaries in the ten parallel sections. The ten parallel sections reveal the non-uniform fault zone geometry of the Lenghu fold-and-thrust belt, with a high level of lateral structural variation along the trend of the structure. The sections through the northern anticline (e.g., sections **S3** and **S4**) represent a fault zone comprising a main reverse fault **F1** and a splay fault **F2** in the footwall. Using ***Sa*** as the reference unit, the main reverse fault **F1** shows a maximum throw of ~450 m that occupies ~90% of the total fault throw, whereas the ~50 m throw of the splay fault **F2** is negligible compared with that of the main reverse fault **F1** (Fig.5). In sections through the southern anticline (e.g., sections **S8** and **S9**), the fault zone still comprises a main reverse fault **F1** and a splay fault **F3**. However, the splay fault **F3** changes to be blind rather than exposed in the surface. An ~850 m cumulative fault throw is present in the fault zone and the main thrust fault **F1** keeps accounting for the majority of the fault throw (Fig.5). The differences between the northern and southern anticlines, with respect to both the cumulative fault throw and fault zone geometry, may be accounted for by the uneven contraction perpendicular to the Lenghu fold-and-thrust belt. Therefore, a geospatial model is essential because it allows quantitative evaluation of fault throw distribution along the Lenghu fold-and-thrust belt.

5. Geospatial Model and three-dimensional Structural Evolution

5.1. Geospatial model and fault throw distribution

The spatial distribution of the fault throw is vital to understand its control on the geometry of hanging-wall anticline and lateral variation of fault zone architecture. By integrating landsat image interpretation, regional stratigraphy, fault system maps and parallel cross sections, the three-dimensional structural geometry of the Lenghu fold-and-thrust belt is visualized in the geospatial model (Fig.6a). In this geospatial model, the main thrust fault (i.e., **F1**) and two large splay faults (e.g., **F2** and **F3**) in the footwall are constructed, whereas the other minor faults in the hanging-wall are simplified. Horizons representing the stratigraphic boundaries between the main stratigraphic packages are generated in the hanging-wall (e.g., ***hb0-hb5***), footwall (e.g., ***hb0-fb5***) and central compartments between the main thrust fault **F1** and splay faults **F2** and **F3**. In order to define the throws of each fault plane, the horizons are also extrapolated above the present topography until they are against the thrust faults.

The Lenghu fold-and-thrust belt is controlled by the thrust fault zone beneath the northern and southern culminations (purple peaks in Fig.6a). The hanging-wall anticline presents a relatively flat crest adjacent to the main thrust fault (**F1**). The fault zone is composed of a single-plane thrust fault (**F1**) and multiple splay faults (e.g., **F2** and **F3** in the footwall), but it presents non-uniform combinations of them along the Lenghu fold-and-thrust belt. The splay fault **F2** is exposed in the surface, whereas the splay fault **F3** is a blind splay that accounts for the development of a pair of tight syncline and open anticline in the southern footwall. These splay faults generate some lenses, which might affect the hydrocarbon sealing properties as compartments are formed within the fault zone. Moreover, a pair of structures, a small-scale tight syncline and open anticline, are developed in the footwall due to the propagation of splay fault **F3**. The geospatial model demonstrates that both the hanging-wall anticline and fault zone present high level of lateral variability from NW to SE along the structure.

The plan view perspective of the thrust fault zone presents the spatial distribution of the main thrust fault and splay faults in the footwall (Fig.6b). The main thrust fault (**F1**) is set translucent to visualize the splay faults (**F2** and **F3**) beneath it. The main fault **F1** extends from the northern end to the southern end of the Lenghu fold-and-thrust belt, whereas the splay faults **F2** and **F3** occur in limited portions along the strike of **F1**. Integrating the three-dimensional geospatial model (Fig.6a) and three-dimensional plain view perspective (Fig.6b), the spatial distribution of fault throw is evaluated in a throw versus distance diagram along the section A-B (Fig.6b, c). In the fault throw distribution diagram, the vertical and horizontal axes represent the fault throw and distance along the fault zone. The fault throw of the main fault (**F1**) and splay faults (**F2** and **F3**) are all measured as well as the cumulative fault throw ($\mathbf{F_{cum}}$). The uneven fault throw distribution apparently demonstrates non-uniform faulting deformation along the Lenghu fold-and-thrust belt. The cumulative fault throw ($\mathbf{F_{cum}}$) along the Lenghu thrust fault zone, ranging from ~300 m to ~850 m, presents the maximum throw in sections **S3** and **S9**, which correspond to the positions of northern and southern culminations in the hanging-wall (Fig.6a). The main thrust fault **F1** presents the fault throw ranging from ~250 m (in section **S5**) to ~650 m (in section **S9**), which occupies 75-85% of the cumulative fault throw. The splay faults **F2** and **F3** present the maximum fault throw of ~80 m (in section **S6**) and ~180 m (in section **S9**), respectively. The cumulative fault throw ($\mathbf{F_{cum}}$) shows positions of highs and lows that are similar to the main thrust fault **F1**, and there are similar trends for the transition between the highs and lows. This indicates that the main thrust fault **F1** determines the primary structural geometry of the Lenghu fold-and-thrust belt, whereas the splay faults (e.g., **F2** and **F3**) only generate the second-order structures (e.g., minor normal faults in the hanging-wall and small folds in the footwall).

5.2. Three-dimensional structural evolution

The progressive faulting deformation is vital to understand the control of the fault system on the development of the Lenghu fold-and-thrust belt. To reveal the kinematic evolution of the Lenghu thrust fault zone, we restored the geospatial model using the modules of '***3D Move-on-Fault***' and '***3D Unfolding***' in the three-dimensional Kinematic Modelling of Midland Valley. The ***3D Move-on-Fault*** tool allows geologists to restore the hanging-wall back to its original position before faulting deformation by eliminating the fault throw between the fault blocks, with the input of the spatial distribution of the fault throw along the fault strike. The ***3D Unfolding*** tool enables geologists to restore a geological horizon to its pre-deformation datum or target surface, with the definition of a pin line in a proper position. Although several different calculating algorithms are available, the calculating algorithms employed in the '***3D Move-on-Fault***' and '***3D Unfolding***' are 'Fault Parallel Flow' and 'Flexural Slip Unfolding', respectively (e.g., Egan et al., 1997; Kane et al., 1997). The ***3D Move-on-Fault*** along faults are quantitatively constrained by the spatial distribution of the fault throw measured in the geospatial model of the Lenghu fold-and-thrust belt (Fig.6). As **F2** and **F3** are splay faults branching off from the main thrust fault **F1**, they were restored prior to the restoration of **F1**. Here we unfolded the layers after restoration of **F1**, **F2** and **F3**, although the hanging-wall anticline could be simultaneously developed during the faulting deformation. The geospatial model of the Lenghu thrust-fold belt was restored by the following steps: (i) erosion restored: by extrapolating the layers until against the faults (Fig.7f→e), (ii) splay fault **F3** restored: by ***Move on Fault*** along **F3** (Fig.7e→d), (iii) splay fault **F2** restored: by ***Move on Fault*** along **F2** (Fig.7d→c), (iv) main fault **F1** restored: by ***Move on Fault*** along **F1** (Fig.7c→b), and (v) folding restored: by ***Unfolding*** the layers (Fig.7b→a).

As the above restoration procedures are reversible, the kinematic evolution of the Lenghu fold-and-thrust belt is reconstructed, in both plain view and three-dimensional perspectives (Fig.7). Based on the progressive faulting/folding deformation, the kinematic evolution of the Lenghu fold-and-thrust belt is drawn as below:

(i) sedimentation of stratigraphic packages ***Sa-Se*** (Fig.7a);

(ii) folding of the layers and initiation of thrust fault **F1** reacting to the NE-SW regional contraction (Fig.7b);

(iii) development of the thrust fault **F1** that is perpendicular to the NE-SW contraction (Fig.7c);

(iv) development of splay faults **F2** and **F3**, branching off from the main thrust fault **F1** to accommodate the overall strain happened in the footwall (Fig.7d, e);

(v) uplift and erosion to present (Fig.7f).

6. Prediction of strain distribution and field data validation

Apart from the main faults (i.e., **F1**, **F2** and **F3**) and primary fold geometry, minor structures such as small faults and folds are also observed in the Lenghu fold-and-thrust belt (e.g., in the white rectangle in Fig.3; see details in Fig.9 and related text). However, these minor structures are apparently simplified when we constructed the geospatial models of the Lenghu fold-and-thrust belt. Although these minor structures have smaller offsets or amplitudes/wavelengths, their development is vital to help understand the strain distribution within a certain structural domain, because the minor structures are normally developed to accommodate the overall strain in the primary structures. Therefore, we compiled geomechanical modelling upon the geospatial model of the Lenghu fold-and-thrust belt to examine the correlation between the predicted strain distribution and the distribution of minor structures observed in the fieldwork.

1) Geomechanical modelling and strain prediction

Here, we used the "***Geomechanical Modelling***" module within 3D Move of Midland Valley, which provides a workflow-managed three-dimensional restoration tool. The geomechanical modelling, using a Mass-Spring algorithm (e.g., Baraff and Witkin, 1998; Bourguignon and Cani, 2000; Provot, 1995; Terzopoulos et al., 1987), provides an effective three-dimensional tool for model validation and advanced structural strain analysis. The Mass-Spring approach is an established and extensively used technique in the discipline of computer graphics, and it is typically used for modelling real-time deformation of rigid and non-rigid bodies. The Mass Spring algorithm is an iterative numerical technique designed to minimize the strain within a solid body while attempting to retain its original shape. The Mass Spring solver is well suited to modelling geological structures because it mimics natural forces using the physical laws of motion. The implementation of the Mass-Spring algorithm in the geomechanical modelling workflow (3D Move, Midland Valley) allows for the customization of spring properties to model isotropic or anisotropic rock deformation at the scale of each element. The Mass-Spring algorithm utilized in geomechanical modelling focuses on the movement of each vertex of the deformed surface and the principle extensional or contractional strain is calculated by evaluating the magnitude of relative movement between the neighboring vertices. After Mass-Spring restoration upon the geospatial model in geomechanical modelling, the resultant strain distribution in the Lenghu fold-and-thrust belt, particularly in the hanging-wall, was investigated to predict the distribution of minor structures.

As the main thrust fault **F1** occupies 85-90% of the cumulative fault throw, we focused on the impact of **F1** in the geomechanical modelling (Fig.8). In the geomechanical modelling, the geospatial model (top surface) was restored to its undeformed state (bottom surface) using the Mass-Spring algorithm. The colored surface (Fig.8a) presents the total movement of each vertex from the original plain surface to the deformed surface. The principle strains of the surface during deformation are tracked (tension positive convention), e.g., extensional principle strain e_1 (Fig.8b), contractional principle strain e_3 (Fig.8c) and strain ratio $(1+e_1)/(1+e_3)$ (Fig.8d). The uneven fault throws determine the non-uniform spatial movement of each vertex in the geomechanical models, e.g., two topographic culminations and a middle saddle in between (Fig.8a). The footwall presents a uniform high contractional strain, whereas the hanging-wall presents a complicated strain distribution due to the uneven fault throw along the thrust fault (Fig.8b, c). Apparently, the two culminations are dominated by extensional strain, whereas the middle saddle is dominated by contractional strain. The strain distribution pattern may generate extensional structures such as normal faults with smaller offsets concentrating around the culminations, which agrees with the field observation that the minor normal faults are 90% concentrated within the hanging-wall anticlines (see the distribution of normal faults in the hanging-wall, in Fig.3). However, as the splay faults were simplified, the geomechanical modelling has not fully integrated the natural complexity of the Lenghu fold-and-thrust belt. Therefore, this strain prediction based on geomechanical modelling can be trusted only after it is validated by natural observations.

2) Field data validation

To validate the strain distribution predicted by the aforementioned geomechanical models, the minor structures in the Lenghu fold-and-thrust belt were mapped in detail to evaluate field strain distribution and its consistency with the strain prediction. A 1 km × 1 km rectangle was selected to map the normal fault arrays, with fault throws ranging from meters to tens of meters (Fig.9, see its position in Fig.3). The hanging-wall anticline is subparallel to the Lenghu thrust fault, presenting a high-angle forelimb and a shallow-angle backlimb. Normal faults are developed almost exclusively in the hanging-wall rather than the footwall, which agrees with the extensional strain dominated hanging-wall and contractional strain dominated footwall predicted by the geomechanical models in Fig.8. These mapped normal faults are mostly high angle faults, with throw ranging from meters to tens of meters. We measured throws for the majority of the mapped faults, except those of which the throw exceeds their own outcrop sizes. The mapped normal fault arrays apparently do not present an even distribution in the hanging-wall, but they primarily localize near the hanging-wall anticline. Normal faults with larger throws (> ~10 m) are mostly N-S-striking, whereas normal faults with smaller throws (< ~10m) are primarily NE-SW-striking.

We also generated strike rose diagrams and stereonets to evaluate the relationship between the normal fault arrays and Lenghu thrust fault (Fig.10). The strike rose diagrams and stereonets predict a mean principle plane for the Lenghu thrust fault and two mean principle planes for the normal fault arrays. The strike rose diagram and stereonet indicates that the Lenghu thrust fault presents a mean principle fault plane of 258°∠60°-75° (Fig.10a, c). Although the normal faults show various strikes, two main sets of the normal faults can be identified in the strike rose diagram, a N-S trending set at ~002°/182° and a NE-SW trending set at ~053°/233°, respectively (Fig.10b). The N-S trending set is sub-parallel to the Lenghu thrust fault, whereas the NE-SW trending set is obliquely truncated by the Lenghu thrust fault (Fig.10c, d). Two sets of normal faults can be distinguished by integrating normal fault arrays map, strike rose diagrams, and stereonets (Fig.9 and Fig.10). The first set is the NE-SW-striking normal faults with throws that mostly do not exceed 10 m (thin red lines in the hanging-wall), and the second set is the N-S-striking normal faults with throws above 10 m (thick red lines in the hanging-wall). Although the NE-SW-striking normal fault arrays present lower fault throws, they have a higher density distribution than the N-S-striking normal fault arrays.

7. Discussion and Conclusions

In this study, we present a case study of applying three-dimensional structural restoration and geomechanical modelling to geospatial models of the Lenghu fold-and-thrust belt. High-resolution field data and landsat images were integrated to construct the geospatial model, which can be used to quantitatively investigate the fault throw changes along the Lenghu thrust fault zone and to understand its control on the lateral structural variation. The geospatial model was then restored in three dimensions to reveal the kinematic evolution of the Lenghu fold-and-thrust belt.

Geomechanical modelling, using a Mass-Spring algorithm (e.g., Baraff and Witkin, 1998; Bourguignon and Cani, 2000; Provot, 1995; Terzopoulos et al., 1987), provided an effective three-dimensional tool for structural strain analysis, which was used to predict the strain distribution throughout the overall structure (e.g., normal faults with throws ranging from meters to tens of meters in the hanging-wall). The strain distribution predicted by geomechanical modelling was then compared with the natural normal faults observed in the fieldwork to validate the applicability of geomechanical modelling. The high accordance between the strain prediction and statistics of natural normal faults indicates good applicability of geomechanical modelling in this complex geological setting. We anticipate that the application of three-dimensional geospatial modelling and geomechanical modelling can provide an effective workflow for investigating the fault architecture at different scales (e.g., ranging from regional- to meso-scale), particularly in the geological setting where traditional geo-data collection and analytical techniques are insufficient to understand the structural complexity and its geological history.

As an important oil-bearing fold-and-thrust belt, many previous studies investigated the structural geometry of the Lenghu fold-and-thrust belt, such as, regional scale section construction, seismic interpretation, and structural restoration (Figure.10 and profile 3 of Figure.13, in Yin et al. (2008a)). Using traditional data collection and analytical techniques (e.g., dip measurements, section construction, and section restoration), Yin et al. (2008a) revealed the first-order geometry of the Lenghu fold-and-thrust belt and fit this regional structure into the basin-scale geological setting. However, constrained by the limitations of these traditional data collection and analytical methods, it is difficult to evaluate the structural deformation at meso-scale. In this study, the application of geospatial and geomechanical models provided new insights into our understanding of the complex geological setting and demonstrated a robust technique for analyzing and interpreting multi-scale geo-data within a three-dimensional environment. In particular, our understanding in the lateral variation of the Lenghu structure (Fig.5), spatial distribution of fault throws (Fig.6), kinematics of the structure (Fig.7), and principle strain distribution (Fig.8) are highly improved with geospatial and geomechanical models. The geospatial and geomechanical models revealed the important control of the fault throw distribution on both the lateral structural variation and strain spatial distribution.

As computer-aided analytical techniques, it is necessary to understand the accuracy of the geospatial models, such as the spatial distribution of fault throw along the Lenghu fold-and-thrust belt. As 3D Move (Midland Valley) provides a quantitative calculation of fault throw based on the juxtaposition relationship between the hanging-wall and footwall, the accuracy of the fault throw distribution depends on both the field data collection and section construction. Apparently, high-resolution field data collection can guarantee accurate input for geospatial models, as well as proper selection of algorithms for section construction. There are also limitations in the current geomechanical models. Although the geomechanical modelling is useful for meso-scale strain prediction, it needs to be recognized that lithology and mechanical strength also play important roles in the resultant strain distribution (e.g., Alonso and Teixell, 1992; Hardy and Finch, 2007; Hardy and Ford, 1997), which has not been considered in the geomechanical modelling at this stage. The current Mass-Spring algorithm utilized in geomechanical modelling only focuses on the movement of each vertex of the deformed surface without considering the impact of lithology or mechanical strength. The principle extensional and contractional strain were also calculated by evaluating the magnitude of relative movement between the neighboring vertices. The effects of stratigraphy on the fault architecture has been widely discussed, and it is commonly agreed that competent stratigraphy is strong and behaves in a brittle fashion whereas weaker stratigraphy inclines to ductile deformation (e.g., Corbett et al., 1987; Couzens and Wiltschko, 1996; Hardy and Finch, 2007; Simpson, 2009). It has been suggested that rocks with high competency usually present higher p/s ratios than low competent rocks (Brandenburg, 2013; Pei et al., 2014; Welch et al., 2009a). Therefore, a sequence of beds comprising weak lithology tend to form a wide fault zone with low density of faults or joints (Erslev, 1991; Welch et al., 2009b), whereas a sequence of beds comprising strong lithology is prior to form a narrower fault zone with a higher density of faults or joints (Childs et al., 1996; Peacock and Sanderson, 1991; Walsh et al., 2003). In regard to a mechanically layered sequence of beds, the resultant distribution of faults or joints has higher complexity (e.g., Welch et al., 2009b). The detailed outcrop studies also suggested that stratigraphy plays an important role in determining the detailed fault architecture at meso-scale and micro-scale (e.g., Loveless et al., 2011; Pei et al., 2015). Many mechanical and physical models suggested the important role of stratigraphy and its strength in controlling the deformation style; however, it is likely to be second-order controls superimposed upon the first-order geometry that are dominated by the throw distribution along a thrust fault (Allmendinger, 1998; Dixon, 2004; Pei et al., 2014; Welch et al., 2009a). Therefore, the resultant strain distribution predicted by geomechanical modelling may not be reliable at a scale that is much smaller than the first-order geometry. We also suggest that field validation could be taken into account as a “ground truthing” tool for geomechanical modelling.

Acknowledgement

We would like to acknowledge Dr Geoff Lloyd, Dr Jonathan Imber, Dr Henry Lickorish, Dr Anren Li and Prof Xin Wang for their helpful communications and suggestions contributing to this research. The support from Qinghai Oilfield of PetroChina and Rock Deformation Research (RDR) is highly appreciated. Thanks are also given to both the section editor Dr Adam Bumby and two anonymous reviewers for their useful and constructive comments that highly improve quality of this manuscript. This research has been collaboratively supported by the National Natural Science Foundation of China (No.41502192, NO.41272142) and Shandong Provincial Natural Science Foundation China (No.2014BSE28008).

Figure Captions

Figure 1 The geological map of the northern Qaidam basin, NE Tibetan Plateau (modified after Yin et al., 2008a). The Qaidam basin is an oil-bearing sedimentary basin developed corresponding to the NE-propagation of stress due to the uplift of the Tibetan Plateau. A series of NW-SE-trending folds and faults are developed in the basin. The study area is located in the NW-SE-trending Lenghu fold-and-thrust belt in the northern Qaidam basin, where a northeast-directing Lenghu thrust fault accounts for the development of the hanging-wall anticline.

Figure 2 The seismic section of the Lenghu fold-and-thrust belt delineating the primary structural geometry (see position in Fig.1) (modified after Pei et al., 2014). Being constrained by the Lengke1 well, horizons and faults are interpreted in the seismic section. Initiating from a horizon-parallel low angle fault, the upper Lenghu thrust (f_1) presents upward-steepening fault geometry. The Lenghu fold-and-thrust belt is dominated by the upper NE-directing Lenghu thrust fault (f_1) and the lower inversed faults (f_2 and f_3). The blue rectangle represents the approximate coverage of the parallel sections (i.e., Fig.5) and geospatial models (i.e., Fig.6-7).

Figure 3 The structural interpretation based on detailed field data integrating high-resolution landsat image. The hanging-wall anticline, Lenghu thrust fault zone and minor faults/folds in both the hanging-wall and footwall are interpreted. Three stratigraphic columns (***HW1***, ***HW2*** and ***FW***) are logged along three traverses that are sub-perpendicular to the structure. Ten sub-parallel regional sections (S1-S10) are constructed to build three-dimensional geospatial models to understand the lateral structural variation of the Lenghu fold-and-thrust belt.

Figure 4 The regional stratigraphy of the Lenghu fold-and-thrust belt (see detailed traverses in Fig.3). The hanging-wall stratigraphy (***HW1*** and ***HW2***) presents good correlation with the footwall stratigraphy (***FW***). By correlating the stratigraphic columns, five major stratigraphic units are sub-divided: (S_a) clay-rich fine sandstone (~175 m); (S_b) fine-medium sandstone (~350 m); (S_c) medium sandstone (10-30 m); (S_d) medium-coarse sandstone (~400 m), and (S_e) coarse sandstone to conglomerate (>250 m).

Figure 5 The parallel cross sections delineating the lateral structural variation of the Lenghu fold-and-thrust belt, using 2D/3D Move (Midland Valley). The NW-SE-striking fault zone composes a main thrust fault (i.e., **F1**) and several splay faults (e.g., **F2** and **F3**). The main thrust fault **F1** is a through-going fault along the Lenghu fold-and-thrust belt, whereas **F2** and **F3** are splay faults with minor throws and limited striking extension.

Figure 6 The geospatial model and fault throw distribution along the strike of the Lenghu fold-and-thrust belt. (a) Geospatial model is constructed integrating the parallel cross sections, using 3D Move (Midland Valley). (b) Plan view perspective of the main thrust fault **F1** and two underlying splay faults **F2** and **F3** (**F1** is set translucent to visualize **F2** and **F3**). (c) Throw vs distance chart of the section A-B demonstrating the fault throw distribution along the Lenghu thrust fault zone.

Figure 7 The kinematic evolution of the Lenghu fold-and-thrust belt revealed by three-dimensional restoration using 3D Move (Midland Valley). The yellow arrows represent direction of the principle contractional stress regarding to the geospatial model at each geological time. (a) undeformed layers; (b) folding and initiation of the Lenghu thrust fault **F1**; (c) layers faulted by the Lenghu thrust fault **F1**; (d-e) **F2** and **F3** branching off from **F1**; (f) uplift and erosion to present.

Figure 8 The strain analysis upon the simplified geospatial model of the Lenghu fold-and-thrust belt, based on the geomechanical modelling using a Mass-Spring algorithm in Midland Valley. The results delineate (a) the total movement, (b) the extensional principle strain $\boldsymbol{e_1}$, (c) the contractional principle strain $\boldsymbol{e_3}$, and (d) the strain ratio $(1+ \boldsymbol{e_1})/(1+ \boldsymbol{e_3})$.

Figure 9 The distribution of the high-angle normal faults in a 1 km × 1 km rectangle in the hanging-wall of the Lenghu fold-and-thrust belt (see position in Fig.3). The normal faults are mapped in high-resolution, with fault throws ranging from meters to tens of meters. The normal faults with fault throws smaller than ~10 m are mostly striking NE-SW, which are at high angle with the Lenghu thrust fault zone, whereas the normal faults with fault throws larger than ~10 m are mostly striking N-S, which are sub-parallel to the strike of the Lenghu thrust fault zone.

Figure 10 The strike rose diagrams and stereonets revealing the relationship between the Lenghu thrust fault and the normal fault arrays in the hanging-wall: (a) strike rose diagram of the Lenghu thrust fault, (b) strike rose diagram of the normal fault arrays, (c) stereonet of the thrust fault planes and poles, (d) stereonet of the normal fault planes and poles. The mean principle poles and mean principle planes for each set of the faults are predicted using the '***Orientation Analysis***' module in Midland Valley.

References

Allmendinger, R.W., 1998. Inverse and forward numerical modeling of trishear fault-propagation folds. Tectonics 17, 640-656.

Alonso, J.L., Teixell, A., 1992. Forelimb Deformation in Some Natural Examples of Fault-Propagation Folds. in K. R. McClay, eds., Thrust Tectonics. Springer Netherlands, 175-180.

Baraff, D., Witkin, A., 1998. Large steps in cloth simulation, Proceedings of the 25th annual conference on Computer graphics and interactive techniques. ACM, pp. 43-54.

Bendick, R., Bilham, R., Freymueller, J., Larson, K., Yin, G., 2000. Geodetic evidence for a low slip rate in the Altyn Tagh fault system. Nature 404, 69-72.

Bourguignon, D., Cani, M.-P., 2000. Controlling Anisotropy in Mass-Spring Systems, in: Magnenat-Thalmann, N., Thalmann, D., Arnaldi, B. (Eds.), Computer Animation and Simulation 2000: Proceedings of the Eurographics Workshop in Interlaken, Switzerland, August 21–22, 2000. Springer Vienna, Vienna, pp. 113-123.

Brandenburg, J., 2013. Trishear for curved faults. J Struct Geol 53, 80-94.

Burchfiel, B.C., Deng, Q., Molnar, P., Royden, L., Wang, Y., Zhang, P., Zhang, W., 1989. Intracrustal detachment within zones of continental deformation. Geology 17, 748-752.

Chen, W.P., Chen, C.Y., Nabelek, J.L., 1999. Present-day deformation of the Qaidam basin with implications for intra-continental tectonics. Tectonophysics 305, 165-181.

Chen, X., Yin, A., Gehrels, G.E., Cowgill, E.S., Grove, M., Harrison, T.M., Wang, X.-F., 2003. Two phases of Mesozoic north-south extension in the eastern Altyn Tagh range, northern Tibetan Plateau. Tectonics 22, n/a-n/a.

Chen, Z.Y., Wang, L.Q., Chen, S.P., Wang, Z.X., 2005. Tectonic model and its deformation feature of Cenozoic in west section of Lenghu structural belt, northern margin of Qaidam basin (in Chinese with English abstract). Xinjiang Petroleum Geology 26, 614-617.

Cheng, F., Jolivet, M., Dupont-Nivet, G., Wang, L., Yu, X., Guo, Z., 2015. Lateral extrusion along the Altyn Tagh Fault, Qilian Shan (NE Tibet): insight from a 3D crustal budget. Terra Nova 27, 416-425.

Cheng, F., Jolivet, M., Fu, S., Zhang, Q., Guan, S., Yu, X., Guo, Z., 2014. Northward growth of the Qimen Tagh Range: A new model accounting for the Late Neogene strike-slip deformation of the SW Qaidam Basin. Tectonophysics 632, 32-47.

Childs, C., Watterson, J., Walsh, J.J., 1996. A model for the structure and development of fault zones. J Geol Soc London 153, 337-340.

Corbett, K., Friedman, M., Spang, J., 1987. Fracture development and mechanical stratigraphy of Austin Chalk, Texas. American Association of Petroleum Geologists Bulletin 71, 17-28.

Couzens, B.A., Wiltschko, D.V., 1996. The control of mechanical stratigraphy on the formation of triangle zones. Bulletin of Canadian Petroleum Geology 44, 165-179.

Cowgill, E., 2007. Impact of riser reconstructions on estimation of secular variation in rates of strike-slip faulting: Revisiting the Cherchen River site along the Altyn Tagh Fault, NW China. Earth Planet Sc Lett 254, 239-255.

Cowgill, E., Arrowsmith, J.R., Yin, A., Wang, X.F., Chen, Z.L., 2004a. The Akato Tagh bend along the Altyn Tagh fault, northwest Tibet 2: Active deformation and the importance of transpression and strain hardening within the Altyn Tagh system. Geol Soc Am Bull 116, 1443-1464.

Cowgill, E., Yin, A., Arrowsmith, J.R., Feng, W.X., Zhang, S.H., 2004b. The Akato Tagh bend along the Altyn Tagh fault, northwest Tibet 1: Smoothing by vertical-axis rotation and the effect of topographic stresses on bend-flanking faults. Geol Soc Am Bull 116, 1423-1442.

Craddock, W.H., Kirby, E., Zheng, D.W., Liu, J.H., 2012. Tectonic setting of Cretaceous basins on the NE Tibetan Plateau: insights from the Jungong basin. Basin Res 24, 51-69.

Cui, Z.Z., Li, Q.S., Wu, C.D., Yin, Z.X., Liu, H.B., 1995. The crustal and deep structure in Golmud-Ejin Qi GGT (in Chinese with English abstract). Acta Geophysica Sinica 38, 28-34.

Deng, J., Wu, Z., Yang, J., Zhao, H., Liu, H., Lai, S., Di, Y., 1995. Crust-mantle petrological structure and deep processes along the Golmud-Ejin Qi geoscience section (in Chinese with English abstract). Acta Geophysica Sinica 38, 144-157.

Dixon, J.M., 2004. Physical (Centrifuge) Modeling of Fold-thrust Shortening Across Carbonate Bank MarginsTiming, Vergence, and Style of Deformation. in K. R. McClay, eds., Thrust tectonics and hydrocarbon systems: American Association of Petroleum Geologists Memoir 82, 223-238.

Egan, S.S., Buddin, T.S., Kane, S.J., Williams, G.D., 1997. Three-dimensional modelling and visualisation in structural geology. New techniques for the restoration and balancing of volumes 1, 67-82.

Erslev, E.A., 1991. Trishear Fault-Propagation Folding. Geology 19, 617-620.

Fielding, E.J., 1996. Tibet uplift and erosion. Tectonophysics 260, 55-84.

Gao, R., Chen, X., Ding, Q., 1995. Preliminary geodynamic model of Goldmud-Ejin Qi geoscience transect (in Chinese with English abstract). Acta Geophysica Sinica 38, 14-27.

Gaudemer, Y., Tapponnier, P., Meyer, B., Peltzer, G., Shunmin, G., Zhitai, C., Huagung, D., Cifuentes, I., 1995. Partitioning of Crustal Slip Between Linked, Active

Faults in The Eastern Qilian Shan, And Evidence For aMajor Seismic Gap, the Tianzhu Gap, on theWestern Haiyuan Fault, Gansu (China). Geophys J Int 120, 599-645.

Hardy, S., Finch, E., 2007. Mechanical stratigraphy and the transition from trishear to kink-band fault-propagation fold forms above blind basement thrust faults: A discrete-element study. Mar Petrol Geol 24, 75-90.

Hardy, S., Ford, M., 1997. Numerical modeling of trishear fault propagation folding. Tectonics 16, 841-854.

Jolivet, M., Brunel, M., Seward, D., Xu, Z., Yang, J., Malavieille, J., Roger, F., Leyreloup, A., Arnaud, N., Wu, C., 2003. Neogene extension and volcanism in the Kunlun Fault Zone, northern Tibet: New constraints on the age of the Kunlun Fault. Tectonics 22, 1-23.

Kane, S.J., Williams, G.D., Buddin, T.S., Egan, S.S., Hodgetts, D., 1997. Flexural-slip based restoration in 3D, a new approach. 1997 AAPG Annual Convention Official Program A 58.

Loveless, S., Bense, V., Turner, J., 2011. Fault architecture and deformation processes within poorly lithified rift sediments, Central Greece. J Struct Geol 33, 1554-1568.

Mao, L., Xiao, A., Zhang, H., Wu, Z., Wang, L., Shen, Y., Wu, L., 2016. Structural deformation pattern within the NW Qaidam Basin in the Cenozoic era and its tectonic implications. Tectonophysics 687, 78-93.

Meng, Q.R., Hu, J.M., Yang, F.Z., 2001. Timing and magnitude of displacement on the Altyn Tagh fault: constraints from stratigraphic correlation of adjoining Tarim and Qaidam basins, NW China. Terra Nova 13, 86-91.

Métivier, F., Gaudemer, Y., Tapponnier, P., Meyer, B., 1998. Northeastward growth of the Tibet plateau deduced from balanced reconstruction of two depositional areas: The Qaidam and Hexi Corridor basins, China. Tectonics 17, 823-842.

Meyer, B., Tapponnier, P., Bourjot, L., Métivier, F., Gaudemer, Y., Peltzer, G., Guo, S., Chen, Z., 2010. Crustal thickening in Gansu-Qinghai, lithospheric mantle subduction, and oblique, strike-slip controlled growth of the Tibet plateau. Geophys J Int 135, 1-47.

Meyer, B., Tapponnier, P., Bourjot, L., Metivier, F., Gaudemer, Y., Peltzer, G., Shunmin, G., Zhitai, C., 1998. Crustal thickening in Gansu-Qinghai, lithospheric mantle subduction, and oblique, strike-slip controlled growth of the Tibet plateau. Geophys J Int 135, 1-47.

Pang, X., Li, Y., Jiang, Z., 2004. Key geological controls on migration and accumulation for hydrocarbons derived from mature source rocks in Qaidam Basin. J Petrol Sci Eng 41, 79-95.

Peacock, D.C.P., Sanderson, D.J., 1991. Displacements, segment linkage and relay ramps in normal fault zones. J Struct Geol 13, 721-733.

Pei, Y., Paton, D.A., Knipe, R.J., 2014. Defining a 3-dimensional trishear parameter space to understand the temporal evolution of fault propagation folds. J Struct Geol 66, 284-297.

Pei, Y., Paton, D.A., Knipe, R.J., Wu, K., 2015. A review of fault sealing behaviour and its evaluation in siliciclastic rocks. Earth-Science Reviews 150, 121-138.

Provot, X., 1995. Deformation constraints in a mass-spring model to describe rigid cloth behaviour, Graphics interface. Canadian Information Processing Society, pp. 147-147.

Qiu, N.S., 2002. Tectono-thermal evolution of the Qaidam Basin, China: evidence from Ro and apatite fission track data. Petrol Geosci 8, 279-285.

Rieser, A.B., Liu, Y.J., Genser, J., Neubauer, F., Handler, R., Friedl, G., Ge, X.H., 2006a. Ar-40/Ar-39 ages of detrital white mica constrain the Cenozoic development of the intracontinental Qaidam Basin, China. Geol Soc Am Bull 118, 1522-1534.

Rieser, A.B., Liu, Y.J., Genser, J., Neubauer, F., Handler, R., Ge, X.H., 2006b. Uniform Permian Ar-40/Ar-39 detrital mica ages in the eastern Qaidam Basin (NW China): where is the source? Terra Nova 18, 79-87.

Roger, F., Jolivet, M., Malavieille, J., 2008. Tectonic evolution of the Triassic fold belts of Tibet. Cr Geosci 340, 180-189.

Simpson, G.D.H., 2009. Mechanical modelling of folding versus faulting in brittle–ductile wedges. J Struct Geol 31, 369-381.

Song, T.G., Wang, X.P., 1993. Structural Styles and Stratigraphic Patterns of Syndepositional Faults in a Contractional Setting - Examples from Quaidam Basin, Northwestern China. American Association of Petroleum Geologists Bulletin 77, 102-117.

Sun, Z.M., Yang, Z.Y., Pei, J.L., Ge, X.H., Wang, X.S., Yang, T.S., Li, W.M., Yuan, S.H., 2005. Magnetostratigraphy of Paleogene sediments from northern Qaidam Basin, China: Implications for tectonic uplift and block rotation in northern Tibetan plateau. Earth Planet Sc Lett 237, 635-646.

Tapponnier, P., Meyer, B., Avouac, J.P., Peltzer, G., Gaudemer, Y., Guo, S.M., Xiang, H.F., Yin, K.L., Chen, Z.T., Cai, S.H., Dai, H.G., 1990. Active Thrusting and Folding in the Qilian-Shan, and Decoupling between Upper Crust and Mantle in Northeastern Tibet. Earth Planet Sc Lett 97, 382-403.

Terzopoulos, D., Platt, J., Barr, A., Fleischer, K., 1987. Elastically deformable models. SIGGRAPH Comput. Graph. 21, 205-214.

Vincent, S.J., Allen, M.B., 1999. Evolution of the Minle and Chaoshui Basins, China: Implications for Mesozoic strike-slip basin formation in Central Asia. Geol Soc Am Bull 111, 725-742.

Walsh, J.J., Bailey, W.R., Childs, C., Nicol, A., Bonson, C.G., 2003. Formation of segmented normal faults: a 3-D perspective. J Struct Geol 25, 1251-1262.

Wang, B.Q., Wang, Q.H., Chen, H.L., Xiao, A.C., 2006a. Three-D mensional structure modeling and structural analysis of the lenghu area on the northern margin of Qaidam basin. Geotectonica et Metallogenia 30, 430-434.

Wang, E., Xu, F.Y., Zhou, J.X., Wan, J.L., Burchfiel, B.C., 2006b. Eastward migration of the Qaidam basin and its implications for Cenozoic evolution of the Altyn Tagh fault and associated river systems. Geol Soc Am Bull 118, 349-365.

Wei, Y., Xiao, A., Wu, L., Mao, L., Zhao, H., Shen, Y., Wang, L., 2016. Temporal and spatial patterns of Cenozoic deformation across the Qaidam Basin, Northern Tibetan Plateau. Terra Nova 28, 409-418.

Welch, M.J., Davies, R.K., Knipe, R.J., Tueckmantel, C., 2009a. A dynamic model for fault nucleation and propagation in a mechanically layered section. Tectonophysics 474, 473-492.

Welch, M.J., Knipe, R.J., Souque, C., Davies, R.K., 2009b. A Quadshear kinematic model for folding and clay smear development in fault zones. Tectonophysics 471, 186-202.

Wittlinger, G., Tapponnier, P., Poupinet, G., Mei, J., Shi, D., Herquel, G., Masson, F., 1998. Tomographic Evidence for Localized Lithospheric Shear Along the Altyn Tagh Fault. Science 282, 74-76.

Wu, L., Xiao, A., Wang, L., Shen, Z., Zhou, S., Chen, Y., Wang, L., Liu, D., Guan, J., 2011. Late Jurassic–Early Cretaceous Northern Qaidam Basin, NW China: Implications for the earliest Cretaceous intracontinental tectonism. Cretaceous Res 32, 552-564.

Xia, W.C., Zhang, N., Yuan, X.P., Fan, L.S., Zhang, B.S., 2001. Cenozoic Qaidam basin, China: A stronger tectonic inversed, extensional rifted basin. American Association of Petroleum Geologists Bulletin 85, 715-736.

Yang, F., Ma, Z., Xu, T., Ye, S., 1992. A Tertiary paleomagnetic stratigraphic profile in Qaidam Basin (in Chinese with English abstract). Acta Petrologica Sinica 13, 97-101.

Yin, A., Dang, Y., Zhang, M., McRivette, M.W., Burgess, W.P., Chen, X., 2007. Cenozoic tectonic evolution of Qaidam basin and its surrounding regions (part 2): Wedge tectonics in southern Qaidam basin and the Eastern Kunlun Range. Geological Society of America Special Papers 433, 369-390.

Yin, A., Dang, Y.Q., Wang, L.C., Jiang, W.M., Zhou, S.P., Chen, X.H., Gehrels, G.E., McRivette, M.W., 2008a. Cenozoic tectonic evolution of Qaidam basin and its surrounding regions (Part 1): The southern Qilian Shan-Nan Shan thrust belt and northern Qaidam basin. Geol Soc Am Bull 120, 813-846.

Yin, A., Dang, Y.Q., Zhang, M., Chen, X.H., McRivette, M.W., 2008b. Cenozoic tectonic evolution of the Qaidam basin and its surrounding regions (Part 3): Structural geology, sedimentation, and regional tectonic reconstruction. Geol Soc Am Bull 120, 847-876.

Yin, A., Harrison, T.M., 2000. Geologic Evolution of the Himalayan-Tibetan Orogen. Earth and Planetary Sciences 28, 211-280.

Yue, Y., Ritts, B.D., Graham, S.A., 2001. Initiation and Long-Term Slip History of the Altyn Tagh Fault. Int Geol Rev 43, 1087-1093.

Yue, Y.J., Ritts, B.D., Graham, S.A., Wooden, J.L., Gehrels, G.E., Zhang, Z.C., 2004. Slowing extrusion tectonics: lowered estimate of post-Early Miocene slip rate for the Altyn Tagh fault. Earth Planet Sc Lett 217, 111-122.

Zhu, L.D., Wang, C.S., Zheng, H.B., Xiang, F., Yi, H.S., Liu, D.Z., 2006. Tectonic and sedimentary evolution of basins in the northeast of Qinghai-Tibet Plateau and their implication for the northward growth of the plateau. Palaeogeography, Palaeoclimatology, Palaeoecology 241, 49-60.

Zuza, A.V., Cheng, X., Yin, A., 2016. Testing models of Tibetan Plateau formation with Cenozoic shortening estimates across the Qilian Shan–Nan Shan thrust belt. Geosphere 12, 501-532.

1 **Figure 1**

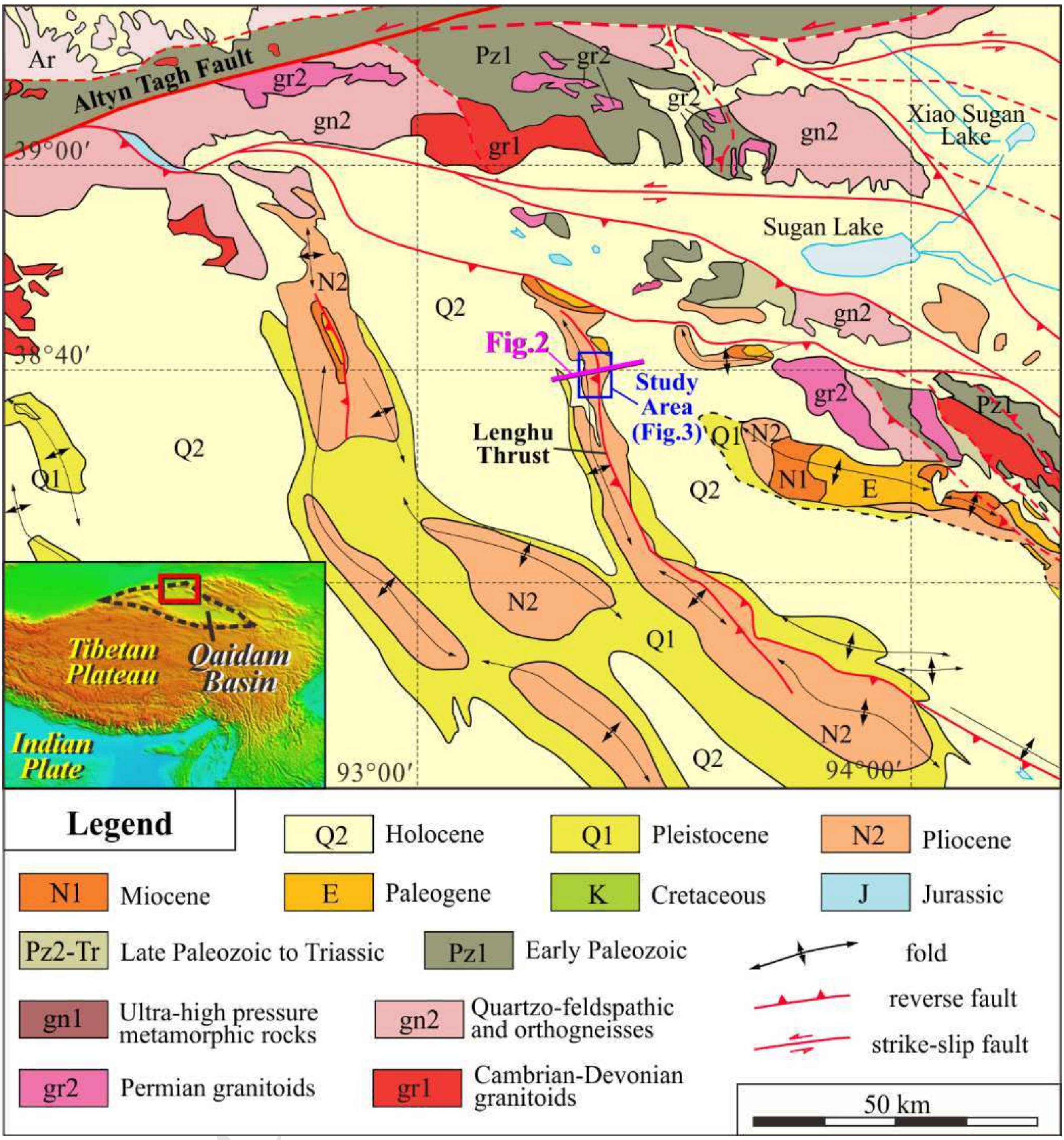
Ar
Altyn Tagh Fault
gr2
gn2
Pz1
gr1
Xiao Sugan Lake
39°00′
Sugan Lake
N2
Q2
38°40′
Fig.2
Study Area (Fig.3)
Lenghu Thrust
Q1
E
N1
Tibetan Plateau
Qaidam Basin
Indian Plate
93°00′
94°00′
Legend
Q2 Holocene
Q1 Pleistocene
N2 Pliocene
N1 Miocene
E Paleogene
K Cretaceous
J Jurassic
Pz2-Tr Late Paleozoic to Triassic
Pz1 Early Paleozoic
fold
gn1 Ultra-high pressure metamorphic rocks
gn2 Quartzo-feldspathic and orthogneisses
reverse fault
strike-slip fault
gr2 Permian granitoids
gr1 Cambrian-Devonian granitoids
50 km

2

3

Figure 2

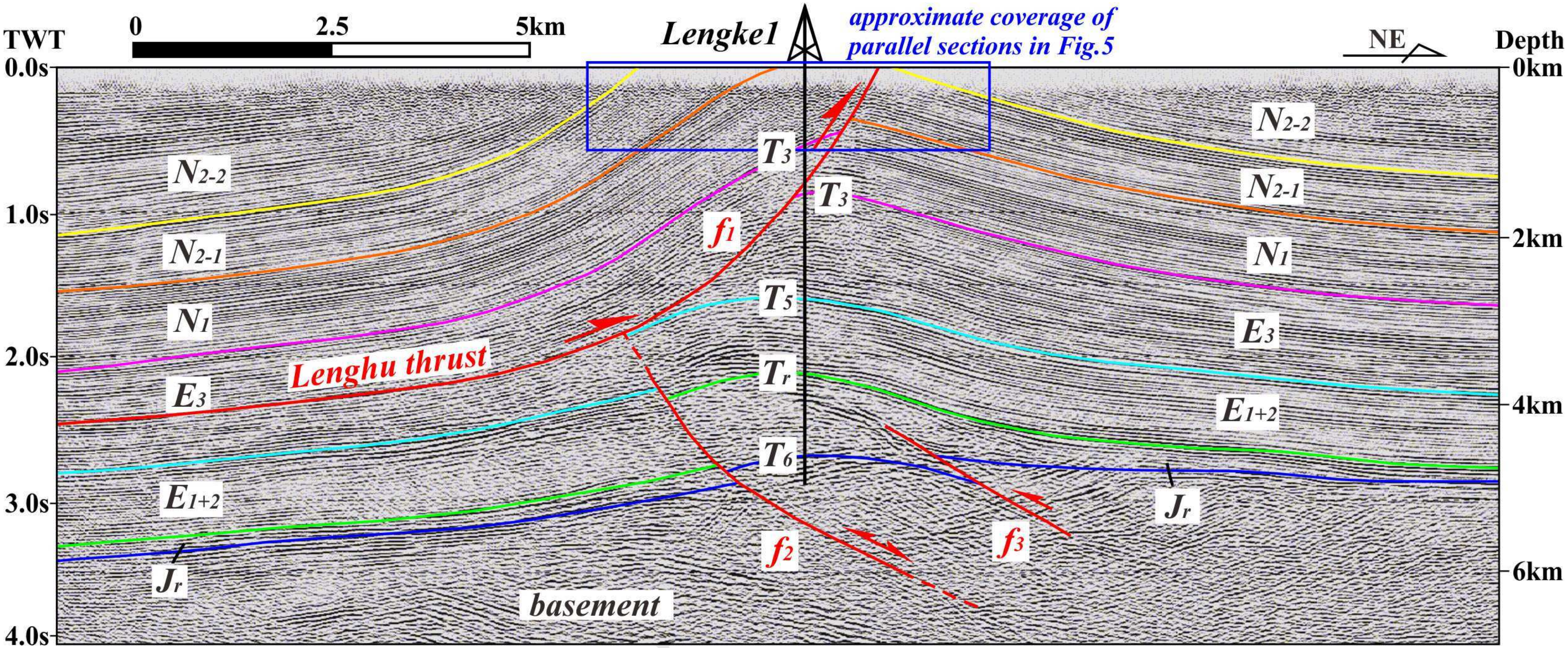
TWT
0
2.5
5km
Lengke1
approximate coverage of
parallel sections in Fig.5
NE
Depth
0.0s
1.0s
2.0s
3.0s
4.0s
0km
2km
4km
6km
N2-2
N2-1
N1
E3
E1+2
Jr
T3
T5
Tr
T6
f1
f2
f3
Lenghu thrust
basement

7 **Figure 3**

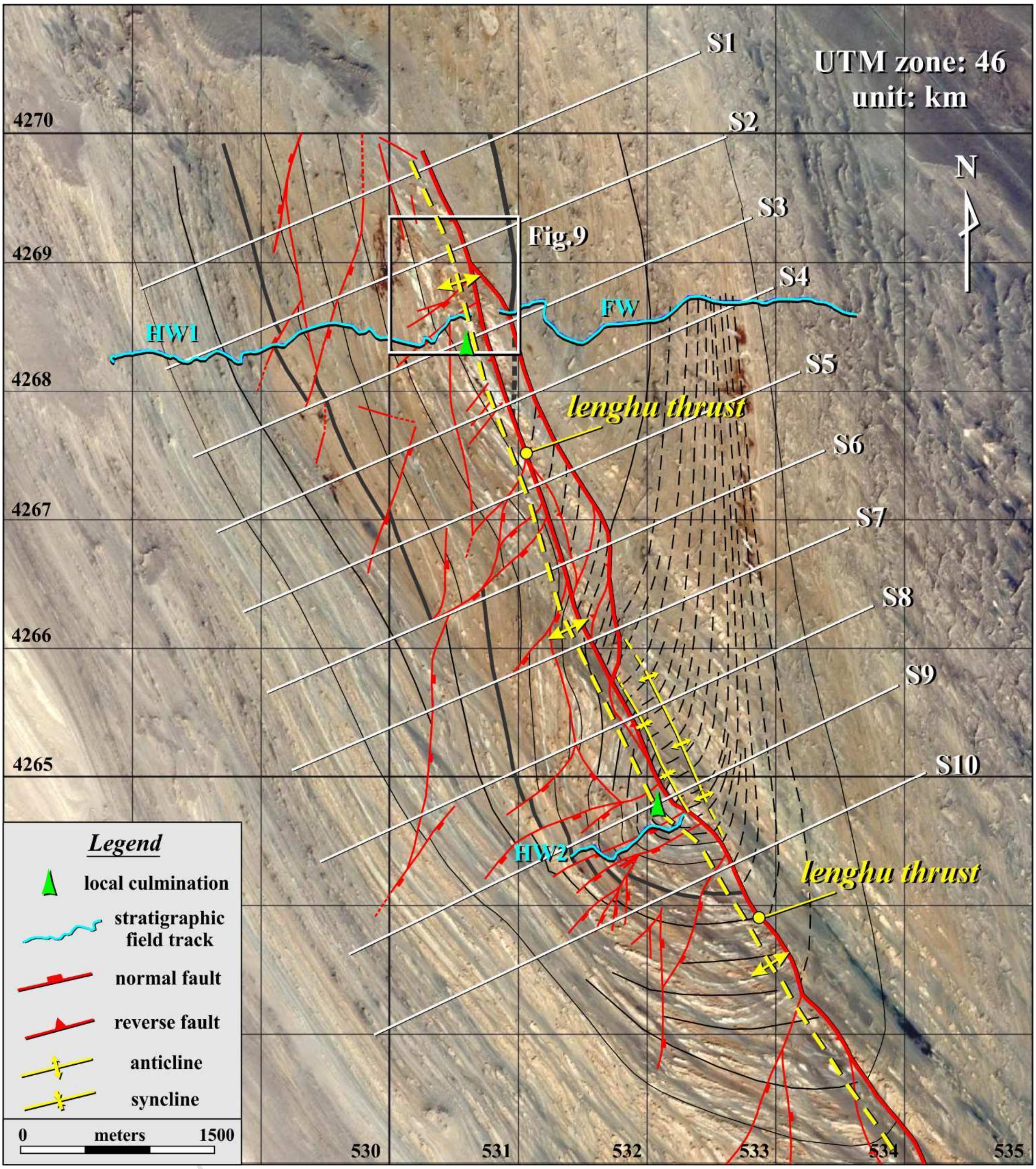
S1
S2
S3
S4
S5
S6
S7
S8
S9
S10
UTM zone: 46
unit: km
N
4270
4269
4268
4267
4266
4265
Fig.9
HW1
FW
HW2
lenghu thrust
lenghu thrust
Legend
local culmination
stratigraphic field track
normal fault
reverse fault
anticline
syncline
0 meters 1500
530
531
532
533
534
535

8

9

Figure 4

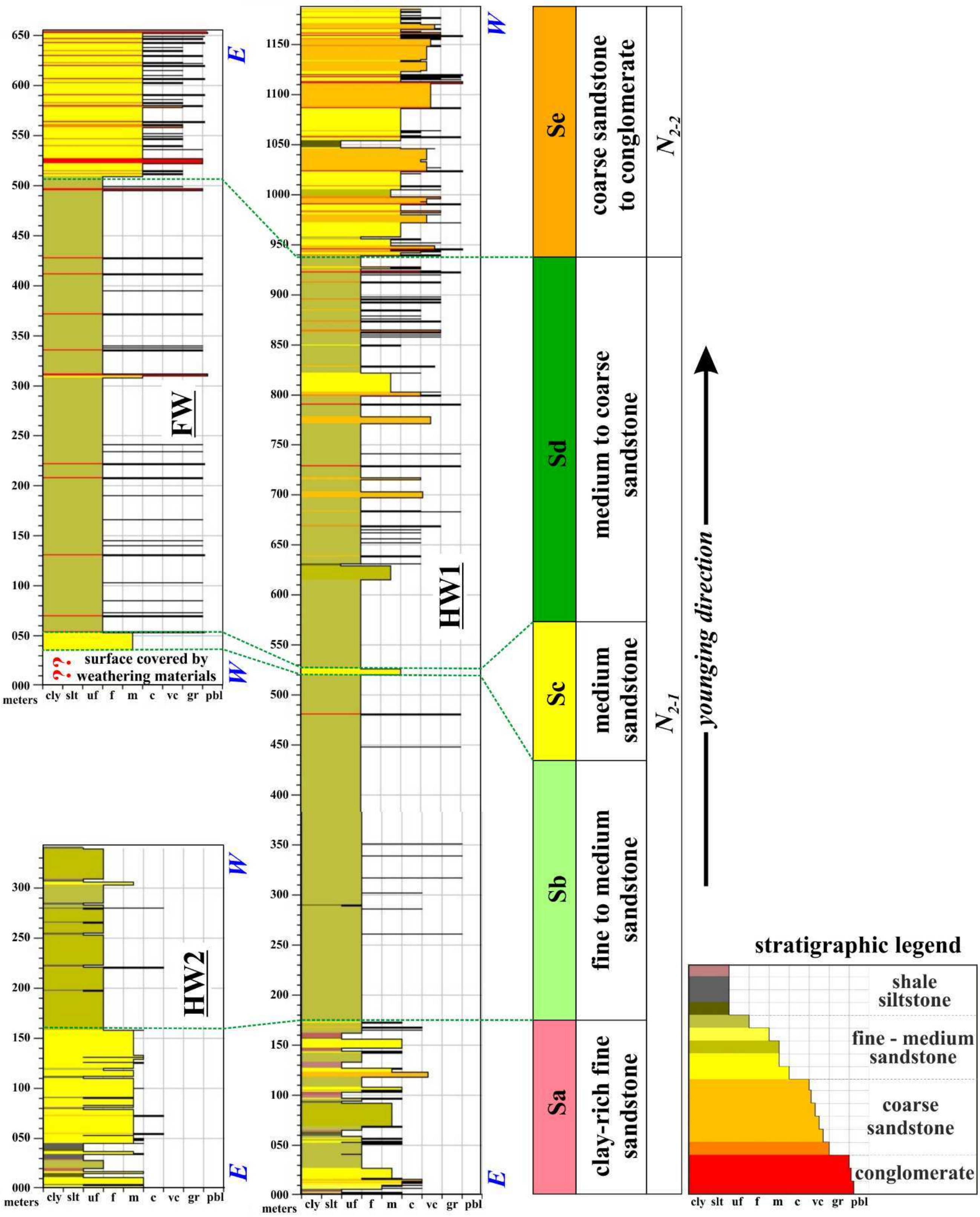
FW
HW1
HW2
E
W
surface covered by weathering materials
meters
cly slt uf f m c vc gr pbl
Se
coarse sandstone to conglomerate
Sd
medium to coarse sandstone
Sc
medium sandstone
Sb
fine to medium sandstone
Sa
clay-rich fine sandstone
N_{2-2}
N_{2-1}
younging direction
stratigraphic legend
shale
siltstone
fine - medium sandstone
coarse sandstone
conglomerate

13 **Figure 5**

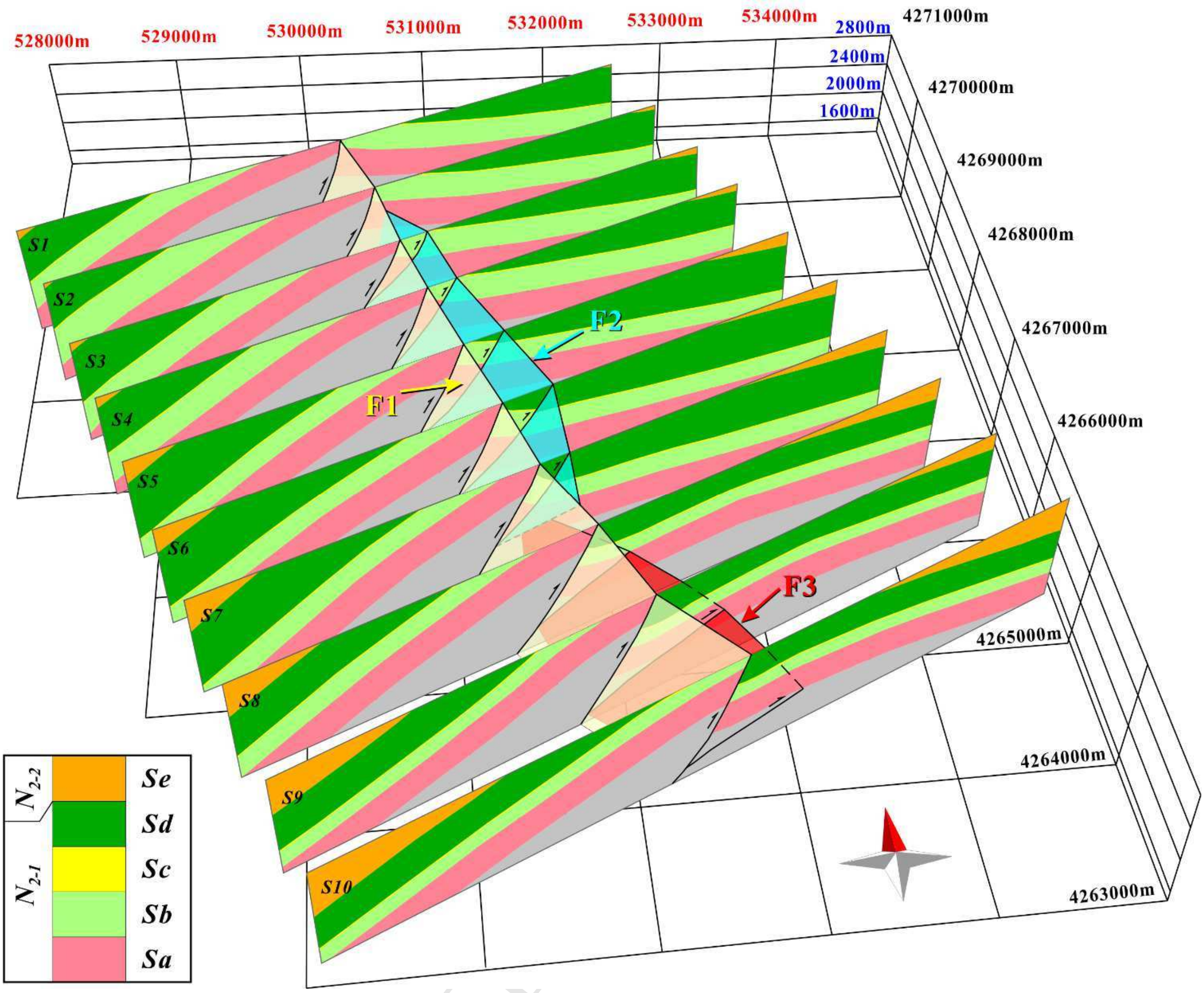

14

15

16 **Figure 6**

17 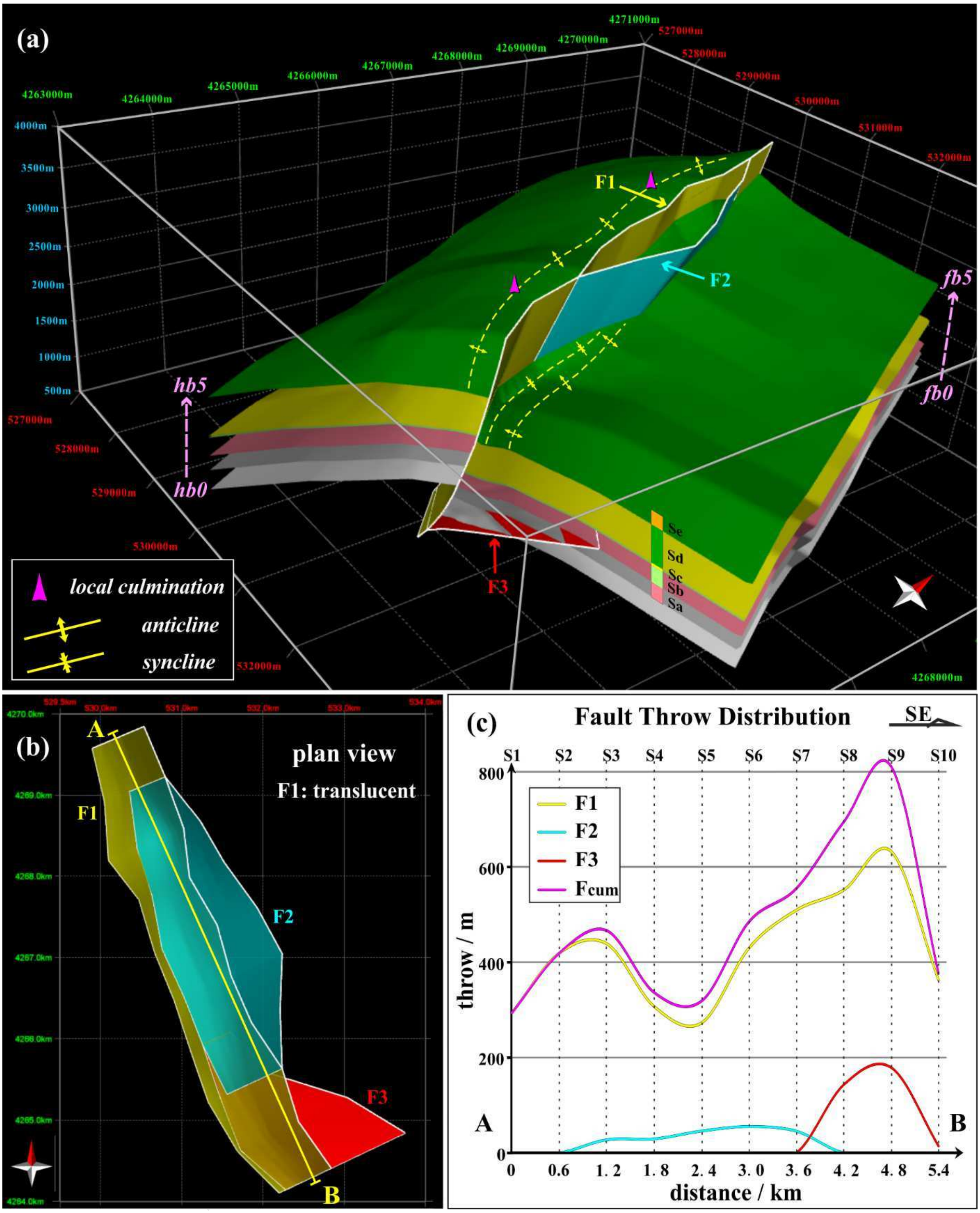

18

Figure 7

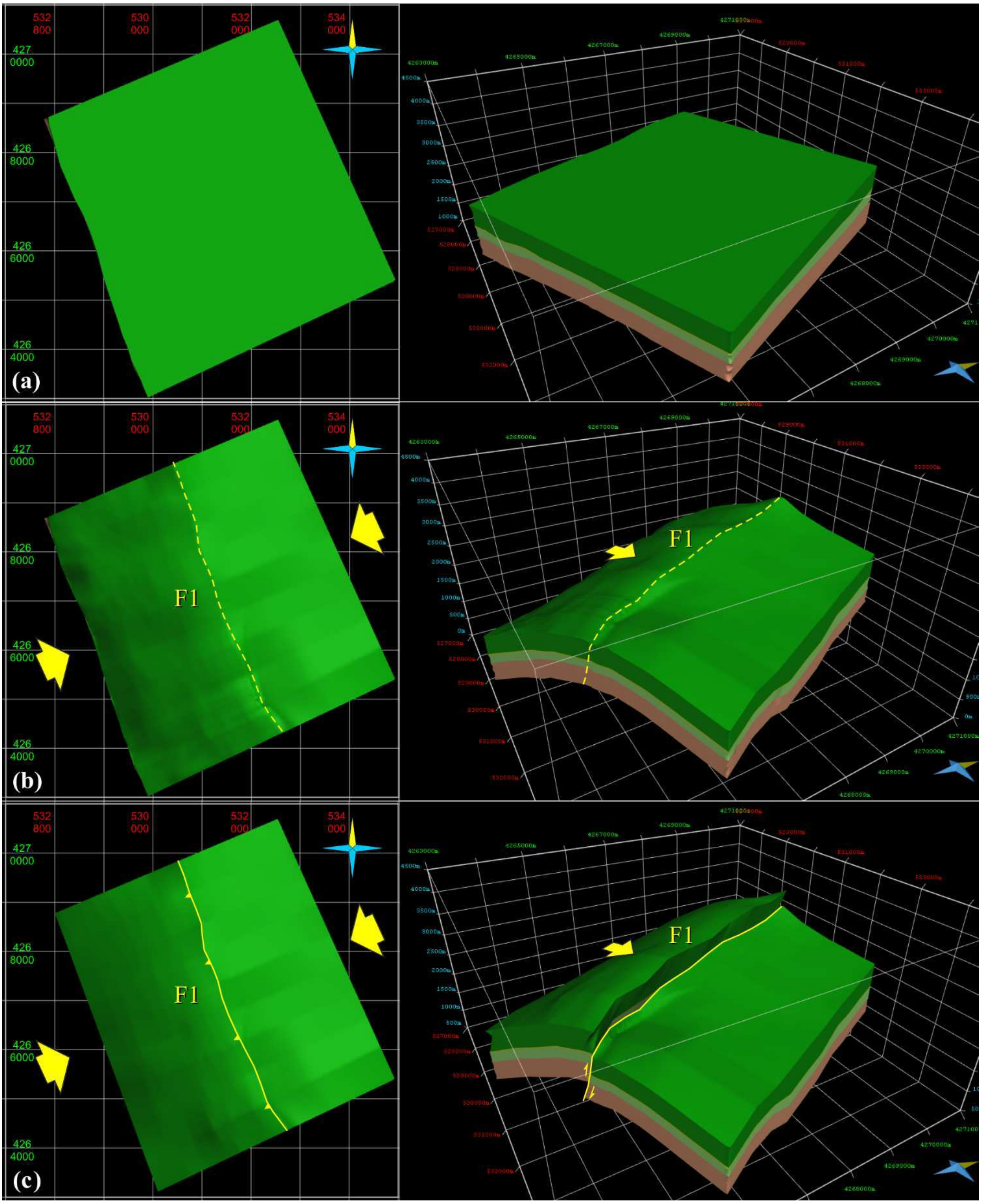

(to be continued)

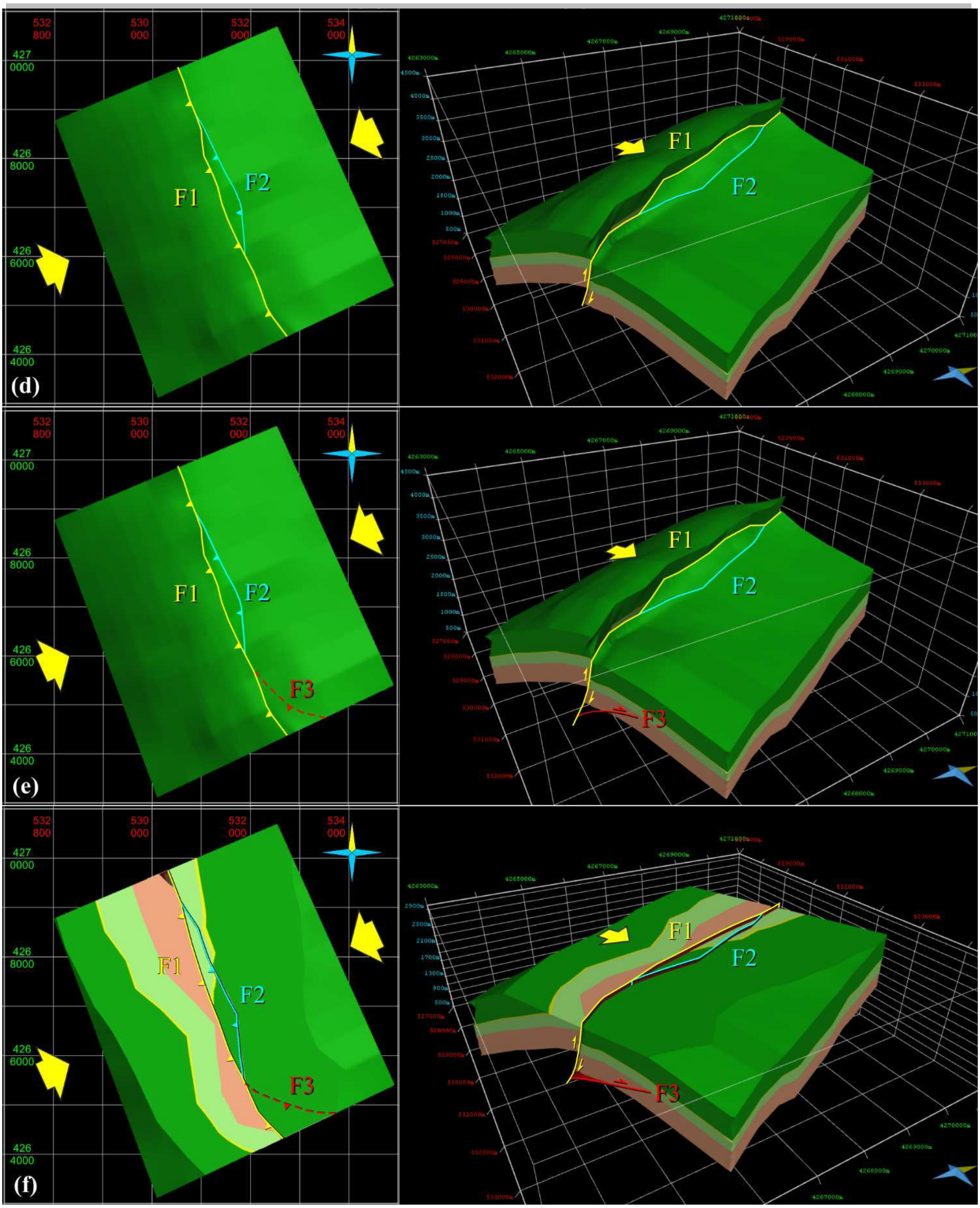

(Figure 7 continued)

26 **Figure 8**

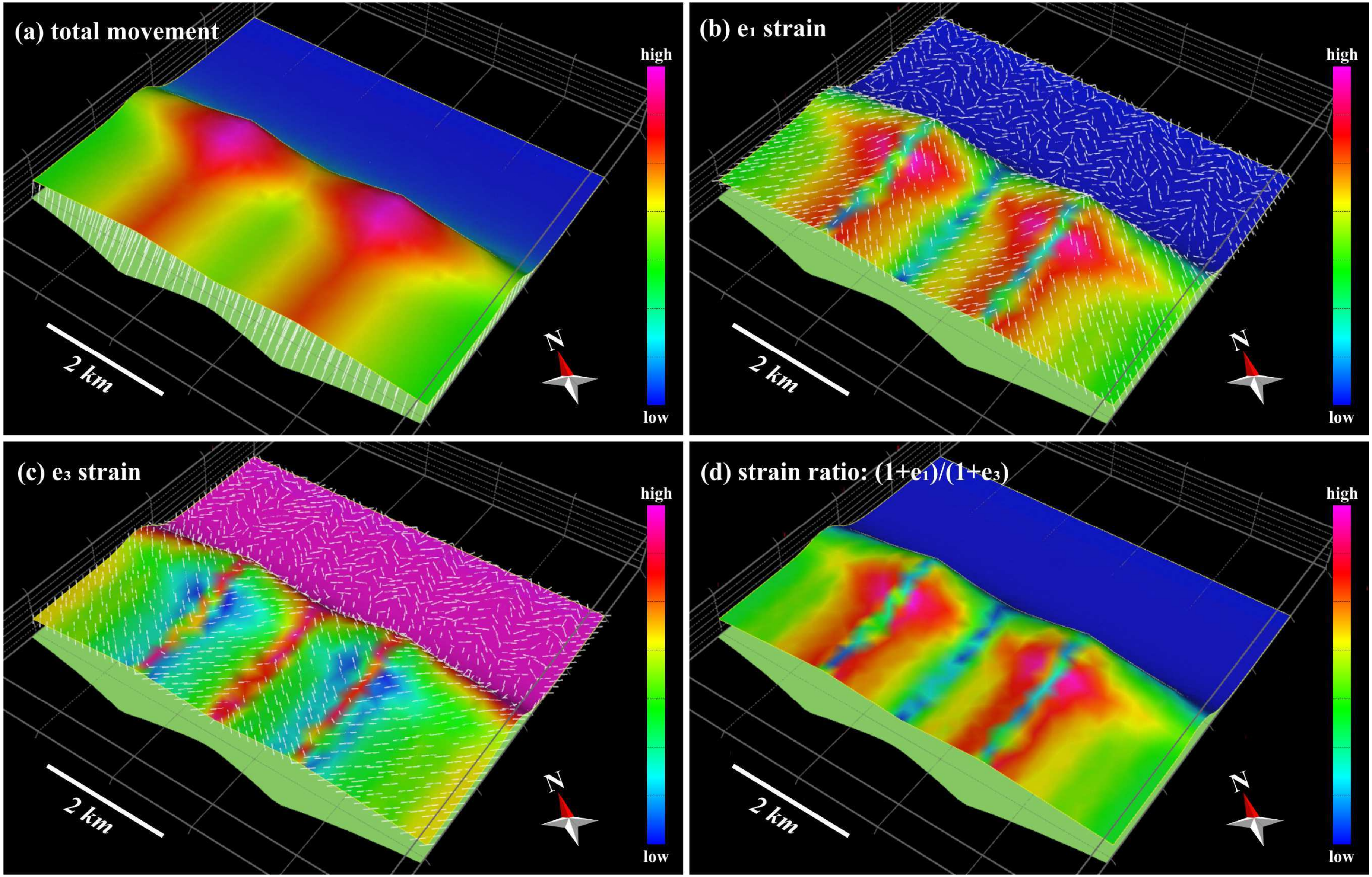

27

Figure 9

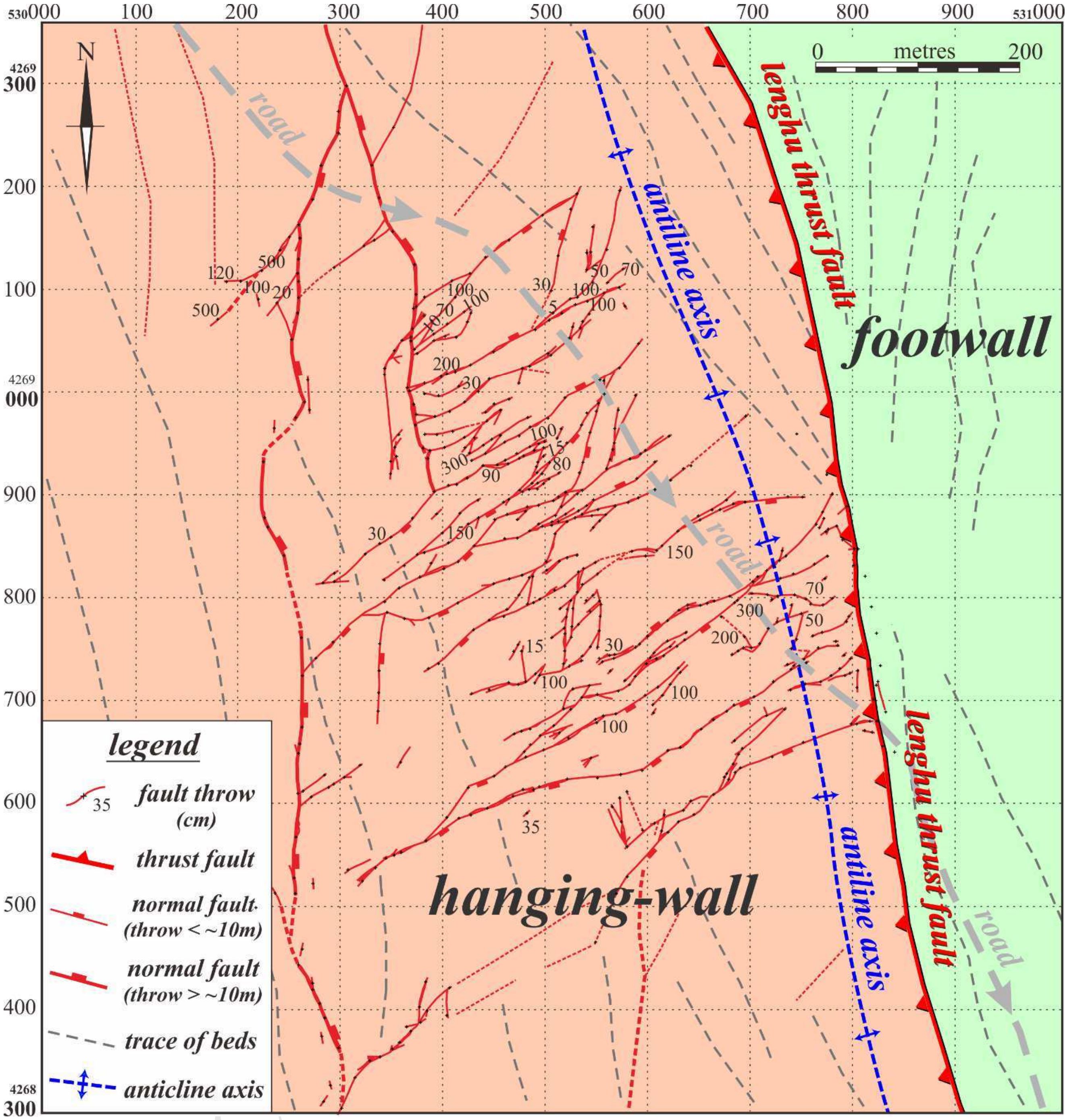

530000
100
200
300
400
500
600
700
800
900
531000
4269 300
200
100
4269 000
900
800
700
600
500
400
4268 300
N
0 metres 200
road
antiline axis
lenghu thrust fault
footwall
hanging-wall
legend
fault throw (cm)
thrust fault
normal fault (throw < ~10m)
normal fault (throw > ~10m)
trace of beds
anticline axis

31 **Figure 10**

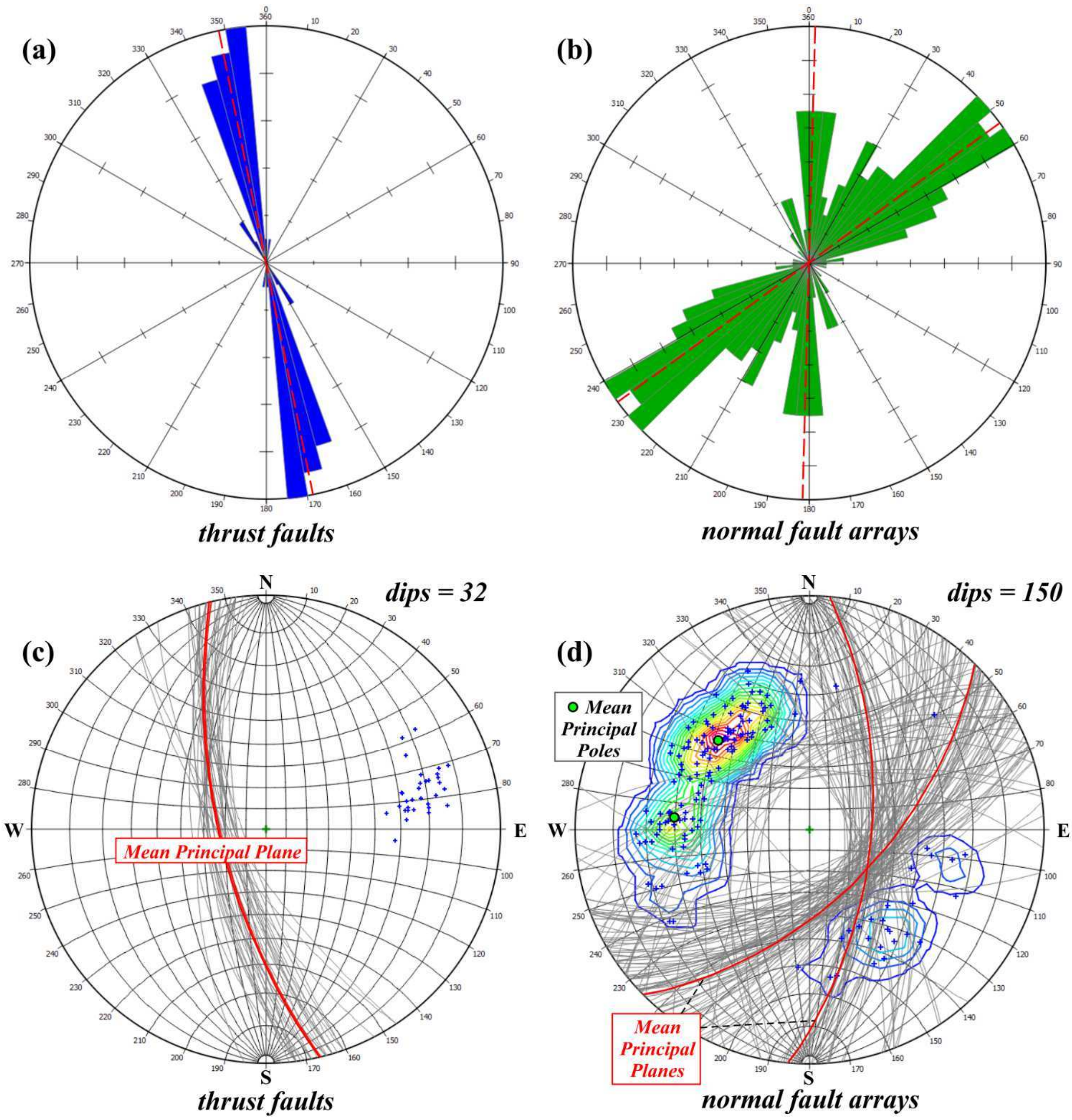

32

Highlights

- The Lenghu fold-and-thrust belt presents high degree of structural variation.
- Geospatial models are constructed based on high-resolution field data.
- Uneven fault throw distribution determines the lateral structural variation.
- Meso-scale strain distribution is predicted using geomechanical modelling.
- Strain prediction needs to be validated by high-resolution field data.